Nuclear ground state properties in a relativistic point coupling model

B. A. Nikolaus* and T. Hoch†
Institut für Kernphysik, Technische Hochschule Darmstadt, D-6100 Darmstadt, Germany and Theoretical Division, Los Alamos National Laboratory, Los Alamos, New Mexico 87545

D. G. Madland
Theoretical Division, Los Alamos National Laboratory, Los Alamos, New Mexico 87545
(Received 16 March 1992)

We present initial results in the calculation of nuclear ground state properties in a relativistic Hartree approximation. Our model consists of Skyrme-type interactions in four-, six-, and eight-fermion point couplings in a manifestly nonrenormalizable Lagrangian, which also contains derivative terms to simulate the finite ranges of the mesonic interactions. A self-consistent procedure has been developed to solve the model equations for several nuclei simultaneously by use of a generalized nonlinear least-squares adjustment algorithm. With this procedure we determine the nine coupling constants of our model so as to reproduce measured ground state binding energies, rms charge radii, and spin-orbit splittings of selected closed major shell and closed subshell nuclei in nondeformed regions. The coupling constants obtained in this way predict these same observables for a much larger set of closed shell spherical nuclei to good accuracy and also predict these quantities for similar nuclei far outside the valley of beta stability. Finally, they yield properties of saturated nuclear matter in agreement with recent relativistic mean meson field approaches.

PACS number(s): 21.60.Jz, 21.10.Dr, 21.10.Ft, 21.10.Gv

I. INTRODUCTION

Relativistic mean field models have been successful in describing nuclear matter and ground state properties of finite nuclei [1–12]. They describe the nucleus as a system of Dirac nucleons that interact in a relativistic covariant manner via mean meson fields. Two important results of these approaches are that the combined meson fields account for the effective central potential used so successfully in Schrödinger approaches and that the spin-orbit interaction occurs naturally, with a magnitude comparable to the *ad hoc* spin-orbit interactions that are required in the Schrödinger approaches.

However, due to the finite range of the mesons it is very difficult to calculate the exchange terms in mean meson field theories, although this has been achieved in Refs. [8] and [9]. A relativistic Hartree-Fock model with Skyrme-type interactions was therefore proposed by Manakos and Mannel [13]. For their four-fermion point coupling interaction, the exchange terms can be calculated via Fierz relations [14]. Although the model is manifestly nonrenormalizable, the question of renormalization of special classes of diagrams and the consistency of the four-fermion interaction is under study [15]. A second concern about the mean meson field theories is that their parametrizations are in terms of mesonic coupling constants and corresponding mesonic masses appearing in the appropriate Klein-Gordon equations (sometimes with additional parameters as coefficients of nonlinear densities). In particular, the Klein-Gordon equation is used to mock-up the exchange of two pions as a (fictitious) stable σ meson because two-pion exchange is believed responsible for the intermediate range attractive part of the nucleon-nucleon interaction [13]. This approach, however, may overly constrain these theories when they are developed at a phenomenological level with intentions of achieving highly accurate predictive capability.

In this work we use an extended version of the relativistic Hartree-Fock model of Manakos and Mannel [13] to describe ground state properties of finite nuclei and nuclear matter. As in the original version, our model Lagrangian contains four-fermion point couplings consisting of squares of scalar and vector densities, with both isoscalar and isovector components. In addition, we include six- and eight-fermion point couplings in the scalar and vector densities together with derivatives of these densities to simulate the finite ranges of the mesonic interactions. However, we have no explicit mean meson fields. Instead, we have mean nucleon fields in a point coupling Skyrme-type approximation. The resulting isoscalar-scalar, isoscalar-vector, isovector-scalar, and isovector-vector potentials have, respectively, four, three, one, and one coupling constants for a total of nine parameters. These potentials can be viewed as corresponding to mean meson fields involving the exchange of σ (fictitious), ω, δ, and ρ mesons, respectively, described by eight pa-

*Present address: Deutsche Bundesbahn, Zentralstelle Datenverabeitung, Gueterstrasse 9, D-6000 Frankfurt 1, Germany.
†Present address: Wersi GmbH and Co., Abteilung Entwicklung, Industriegebiet, D-5401 Halsenbach, Germany.

 ©1992 The American Physical Society

rameters (four coupling constants and four meson masses).

We determine the coupling constants of our model by use of a self-consistent solver of the Hartree equations as the function call in a generalized nonlinear least-squares adjustment algorithm that acts on several nuclei simultaneously. The experimental ground state observables appearing in the χ^2 are (1) the binding energy, (2) the rms charge radius, (3) the spin-orbit energy splitting of the least-bound neutron spin-orbit pair, and (4) the spin-orbit energy splitting of the least-bound proton spin-orbit pair, for each of the chosen nuclei. With the nine coupling constants so determined, we are able to test the model by predicting the same observables for other nuclei and by calculating the properties of saturated nuclear matter. Our early work on developing this approach has been reported in Refs. [16] and [17].

The paper is structured as follows. A summary of the relativistic point coupling model is given in Sec. II. Included are discussions of our approximations, and their justification, together with explicit expressions for the densities and potentials appearing as well as for the ground state binding energy and rms radii. In Sec. III we discuss the method of determining the optimal values of the nine coupling constants of the model. The choice of nuclei, and the corresponding measured observables and their weights, that are used in the generalized nonlinear least-squares algorithm are given. Our results are presented in Sec. IV. Here we tabulate our best set of coupling constants to date determined in the nonlinear least-squares analysis, and compare measured and calculated observables using these coupling constants. The corresponding densities and potentials are also shown. In Sec. V we turn to predictions using the same optimal set of coupling constants and present comparisons of measured and predicted observables for a number of nuclei. We also present predictions for these same observables, together with corresponding densities and potentials, for some exotic nuclei. Finally, our predictions for nuclear matter are given. A discussion and our conclusions are presented in Sec. VI.

II. SUMMARY OF MODEL

In this section we present a description of the relativistic point coupling model introduced by Manakos and Mannel [13,15]. We use units in which $\hbar = c = 1$.

A. Relativistic Lagrangian

The model is defined by a relativistic Lagrangian density in the nucleon fields and does not contain any meson fields. The Lagrangian is given by

$$\mathcal{L} = :\{\mathcal{L}_{\text{free}} + \mathcal{L}_{4f} + \mathcal{L}_{\text{hot}} + \mathcal{L}_{\text{der}} + \mathcal{L}_{\text{em}}\}: , \tag{1}$$

where

$$\begin{aligned}
\mathcal{L}_{\text{free}} &= \bar{\psi}(i\gamma_\mu \partial^\mu - m)\psi , \\
\mathcal{L}_{4f} &= -\tfrac{1}{2}\alpha_S(\bar{\psi}\psi)(\bar{\psi}\psi) - \tfrac{1}{2}\alpha_V(\bar{\psi}\gamma_\mu\psi)(\bar{\psi}\gamma^\mu\psi) \\
&\quad - \tfrac{1}{2}\alpha_{TS}(\bar{\psi}\tau\psi)\cdot(\bar{\psi}\tau\psi) \\
&\quad - \tfrac{1}{2}\alpha_{TV}(\bar{\psi}\tau\gamma_\mu\psi)\cdot(\bar{\psi}\tau\gamma^\mu\psi) , \\
\mathcal{L}_{\text{hot}} &= -\tfrac{1}{3}\beta_S(\bar{\psi}\psi)^3 - \tfrac{1}{4}\gamma_S(\bar{\psi}\psi)^4 \\
&\quad - \tfrac{1}{4}\gamma_V[(\bar{\psi}\gamma_\mu\psi)(\bar{\psi}\gamma^\mu\psi)]^2 , \\
\mathcal{L}_{\text{der}} &= -\tfrac{1}{2}\delta_S(\partial_\nu\bar{\psi}\psi)(\partial^\nu\bar{\psi}\psi) \\
&\quad - \tfrac{1}{2}\delta_V(\partial_\nu\bar{\psi}\gamma_\mu\psi)(\partial^\nu\bar{\psi}\gamma^\mu\psi) ,
\end{aligned} \tag{2}$$

and

$$\mathcal{L}_{\text{em}} = -eA_\mu\bar{\psi}[(1-\tau_3)/2]\gamma^\mu\psi - \tfrac{1}{4}F_{\mu\nu}F^{\mu\nu} .$$

In these equations, ψ is the nucleon field, m is the nucleon mass, the subscripts "S" and "V" refer to the scalar and vector nucleon fields, respectively, the subscript "T" refers to isovector fields containing the nucleon isospin τ, and A_μ and $F_{\mu\nu}$ are the four-vector potential and field strength tensor, respectively, of the electromagnetic field. [Note that throughout this paper, the magnitude of τ is twice the nucleon isospin.] Furthermore, the physical makeup of $\mathcal{L}$ is that $\mathcal{L}_{\text{free}}$ is the kinetic term of the nucleons and $\mathcal{L}_{4f}$ is a four-fermion interaction, while $\mathcal{L}_{\text{hot}}$ and $\mathcal{L}_{\text{der}}$ contain higher-order terms and derivatives in the nucleon densities, respectively. Finally, $\mathcal{L}_{\text{em}}$ is responsible for the coupling of the nucleons to the electromagnetic field and contains its kinetic term.

The four-fermion interaction and the higher-order terms are point coupling interactions made up of the operators of the scalar and vector (both isoscalar and isovector) nucleon densities. The isoscalar operators are $\bar{\psi}(x)\psi(x)$ for the scalar case and $\bar{\psi}(x)\gamma_\mu\psi(x)$ for the vector case. The corresponding isovector operators are $\bar{\psi}(x)\tau\psi(x)$ and $\bar{\psi}(x)\tau\gamma_\mu\psi(x)$. As can be seen from the coupling to the electromagnetic field, we use the nuclear physics convention for the isospin, i.e., the neutron has isospin "up," $\tau_3 = +1$, and the proton has isospin "down," $\tau_3 = -1$. Thus, all spinors are to be understood as having first the neutron part and then the proton part. The colons in Eq. (1) denote a normal ordering with respect to the vacuum state $|0\rangle$. That is, in all expressions between the colons, creation operators are written on the left and destruction operators are written on the right (including a minus sign for each transposition of fermion operators).

In the following, the Lagrangian Eq. (1) is treated in a no-sea approximation, which means that we consider only positive energy states. In other words, the field operator $\psi(x)$ contains only nucleon annihilation operators and no antinucleon creation operators:

$$\psi(x) = \sum_k u_k(x)a_k , \quad \bar{\psi}(x) = \sum_k \bar{u}_k(x)a_k^\dagger , \tag{3}$$

where a_k is the annihilation operator for a nucleon in state k, $u_k(x)$ is the corresponding single-particle Dirac four-spinor wave function with upper and lower com-

ponents $g(x)$ and $f(x)$, and the bar indicates the Dirac adjoint $\bar{u}(x)=u^{\dagger}(x)\gamma_0$.

The field theory defined by Eq. (1) is nonrenormalizable. However, it is possible to treat it in Hartree-Fock (HF) approximation.

B. Relativistic Hartree-Fock and Hartree approximations

Hartree-Fock approximation means that the expectation value $\langle\phi|H|\phi\rangle$ of the Hamiltonian H is to be minimized in the space of Slater determinants

$$|\phi\rangle=\prod_{k=1}^{A} a_k^{\dagger}|0\rangle \ , \tag{4}$$

where A is the nuclear mass number.

The Hamiltonian can be calculated from the relativistic Lagrangian by

$$H=\int d^3\mathbf{x}\,\mathcal{H}(x) \ ,$$

where

$$\mathcal{H}(x)=\frac{\partial\mathcal{L}}{\partial\dot{\psi}(x)}\dot{\psi}(x)+\frac{\partial\mathcal{L}}{\partial\dot{A}_{\mu}(x)}\dot{A}_{\mu}(x)-\mathcal{L}(x) \ . \tag{5}$$

Inserting the Lagrangian, one obtains

$$H=\int d^3\mathbf{x}:\{\mathcal{H}_{\text{free}}(x)+\mathcal{H}_{4f}(x)+\mathcal{H}_{\text{hot}}(x)+\mathcal{H}_{\text{der}}(x)+\mathcal{H}_{\text{em}}(x)\}: \ , \tag{6}$$

where

$$\begin{aligned}
&\mathcal{H}_{\text{free}}=\bar{\psi}(i\boldsymbol{\gamma}\cdot\boldsymbol{\partial}+m)\psi \ ,\\
&\mathcal{H}_{4f}=\tfrac{1}{2}\alpha_S(\bar{\psi}\psi)(\bar{\psi}\psi)+\tfrac{1}{2}\alpha_V(\bar{\psi}\gamma_{\mu}\psi)(\bar{\psi}\gamma^{\mu}\psi)+\tfrac{1}{2}\alpha_{TS}(\bar{\psi}\tau\psi)\cdot(\bar{\psi}\tau\psi)+\tfrac{1}{2}\alpha_{TV}(\bar{\psi}\tau\gamma_{\mu}\psi)\cdot(\bar{\psi}\tau\gamma^{\mu}\psi) \ ,\\
&\mathcal{H}_{\text{hot}}=\tfrac{1}{3}\beta_S(\bar{\psi}\psi)^3+\tfrac{1}{4}\gamma_S(\bar{\psi}\psi)^4+\tfrac{1}{4}\gamma_V[(\bar{\psi}\gamma_{\mu}\psi)(\bar{\psi}\gamma^{\mu}\psi)]^2 \ ,\\
&\mathcal{H}_{\text{der}}=-\tfrac{1}{2}\delta_S[(\partial_0\bar{\psi}\psi)^2+(\boldsymbol{\partial}\bar{\psi}\psi)^2]-\tfrac{1}{2}\delta_V[(\partial_0\bar{\psi}\gamma_{\mu}\psi)^2+(\boldsymbol{\partial}\bar{\psi}\gamma_{\mu}\psi)^2] \ , \text{ and}\\
&\mathcal{H}_{\text{em}}=eA_{\mu}\bar{\psi}[(1-\tau_3)/2]\gamma^{\mu}\psi-F^{0\mu}\partial^0A_{\mu}+\tfrac{1}{4}F_{\mu\nu}F^{\mu\nu} \ .
\end{aligned} \tag{7}$$

The expectation value of H can be calculated using Wick's theorem by means of which expectation values of products of many field operators can be expressed in terms of expectation values of only two field operators (contractions). For example,

$$\begin{aligned}
\langle\phi|:(\bar{\psi}\psi)^2:|\phi\rangle&=\langle\phi|\bar{\psi}_{\alpha}\bar{\psi}_{\beta}\psi_{\beta}\psi_{\alpha}|\phi\rangle\\
&=\langle\phi|\bar{\psi}_{\alpha}\psi_{\alpha}|\phi\rangle\langle\phi|\bar{\psi}_{\beta}\psi_{\beta}|\phi\rangle\\
&\quad-\langle\phi|\bar{\psi}_{\alpha}\psi_{\beta}|\phi\rangle\langle\phi|\bar{\psi}_{\beta}\psi_{\alpha}|\phi\rangle \ .
\end{aligned} \tag{8}$$

In this case, Wick's theorem leads to the well-known direct and exchange terms. There are techniques to express these exchange terms in a form that is identical to the direct terms of products of other densities [15]. Also, the exchange parts of the higher-order terms can be expressed as direct terms of products of these densities using Fierz relations, but these terms are much more complicated than in the case of four-fermion couplings. However, the fact that higher order exchange terms can be expressed as direct terms means, in principle, that a Lagrangian $\mathcal{L}$ can be determined in a relativistic Hartree sense that is equivalent to that determined in a relativistic Hartree-Fock sense, $\mathcal{L}'$. By equivalent, here, it is meant that

$$\langle\mathcal{H}(\mathcal{L})\rangle_{\text{Hartree}}=\langle\mathcal{H}(\mathcal{L}')\rangle_{\text{Hartree-Fock}} \ . \tag{9}$$

Equation (9) is satisfied for a point coupling model provided that (a) all possible Lorentz invariants arising at the Hartree level are included, and (b) that an appropriate approximation is made for the (long-range) Coulomb exchange term. In the initial version of our point coupling model, however, we consider only scalar and vector fields and have, for example, not yet included a tensor field. Accordingly, in the following we will use only the direct terms; that is, we make a relativistic Hartree approximation. The expectation values which then occur are the following:

$$\begin{aligned}
\rho_S(x)&=\langle\phi|\bar{\psi}(x)\psi(x)|\phi\rangle\\
&=\sum_{k=1}^{A}\bar{u}_k(x)u_k(x) \ ,\\
j_{V_{\mu}}(x)&=\langle\phi|\bar{\psi}(x)\gamma_{\mu}\psi(x)|\phi\rangle\\
&=\sum_{k=1}^{A}\bar{u}_k(x)\gamma_{\mu}u_k(x) \ ,\\
\rho_{TS}(x)&=\langle\phi|\bar{\psi}(x)\tau\psi(x)|\phi\rangle\\
&=\sum_{k=1}^{A}\bar{u}_k(x)\tau u_k(x) \ ,
\end{aligned}$$

and

$$\begin{aligned}
\mathbf{j}_{TV_{\mu}}(x)&=\langle\phi|\bar{\psi}(x)\tau\gamma_{\mu}\psi(x)|\phi\rangle\\
&=\sum_{k=1}^{A}\bar{u}_k(x)\tau\gamma_{\mu}u_k(x) \ .
\end{aligned} \tag{10}$$

These nucleon densities are, respectively, the isoscalar-scalar density, the isoscalar-vector current density, the isovector-scalar density, and the isovector-vector current density. For convenience we also define the proton (charge) current density:

$$j^p_\mu(x)=\langle\phi|\bar\psi(x)\frac{1-\tau_3}{2}\gamma_\mu\psi(x)|\phi\rangle=\sum_{k=1}^{A}\bar u_k(x)\frac{1-\tau_3}{2}\gamma_\mu u_k(x)=\tfrac{1}{2}[j_{V_\mu}(x)-j_{TV_{\mu 3}}(x)]\ . \tag{11}$$

Using Eqs. (10) and (11), the expectation value of H is given by

$$\begin{aligned}\langle\phi|H|\phi\rangle=\int d^3\mathbf{x}\Big\{&\sum_{k=1}^{A}\bar u_k(i\boldsymbol\gamma\cdot\boldsymbol\partial+m)u_k+\tfrac{1}{2}\alpha_S\rho_S^2+\tfrac{1}{2}\alpha_V j_{V_\mu}j_V^\mu+\tfrac{1}{2}\alpha_{TS}\boldsymbol\rho_{TS}^2+\tfrac{1}{2}\alpha_{TV}\mathbf{j}_{TV_\mu}\mathbf{j}^\mu_{TV}+\tfrac{1}{3}\beta_S\rho_S^3+\tfrac{1}{4}\gamma_S\rho_S^4\\&+\tfrac{1}{4}\gamma_V(j_{V_\mu}j_V^\mu)^2-\tfrac{1}{2}\delta_S[(\partial_0\rho_S)^2+(\boldsymbol\partial\rho_S)^2]-\tfrac{1}{2}\delta_V[(\partial_0 j_{V_\mu})(\partial_0 j_V^\mu)+(\boldsymbol\partial j_{V_\mu})\cdot(\boldsymbol\partial j_V^\mu)]\\&+eA_\mu j^{p\mu}-F^{0\mu}\partial^0A_\mu+\tfrac{1}{4}F_{\mu\nu}F^{\mu\nu}\Big\}\ .\end{aligned} \tag{12}$$

Minimizing $\langle\phi|H|\phi\rangle$ with respect to the wave functions u_k and using the fact that the ground state is stationary, we obtain the time-independent Hartree equations that are of Dirac type:

$$\begin{aligned}\{&i\boldsymbol\gamma\cdot\boldsymbol\partial+m+\alpha_S\rho_S+\alpha_V\rho_V\gamma_0+\alpha_{TS}\rho_{TS}\tau_3+\alpha_{TV}\rho_{TV}\tau_3\gamma_0\\&+\beta_S\rho_S^2+\gamma_S\rho_S^3+\gamma_V\rho_V^3\gamma_0+\delta_S\Delta\rho_S+\delta_V\Delta\rho_V\gamma_0+eA_0[(1-\tau_3)/2]\}u_k=\gamma_0\varepsilon_k u_k\ .\end{aligned} \tag{13}$$

Here we have used the fact that the isospin of the nucleons is in the 3-direction and have introduced the abbreviations

$$\rho_V=j_{V_0},\quad \rho_{TS}=\rho_{TS_3},\quad \rho_{TV}=j_{TV_{03}}\ . \tag{14}$$

(Note that henceforth we shall refer to a "current density" simply as a "density.") The eigenvalue ε_k in the Dirac equation is the single-particle energy. For the electromagnetic potential, we find the usual Poisson equation:

$$\Delta A_0=4\pi e j_0^p\ . \tag{15}$$

By introducing the isoscalar-scalar and isoscalar-vector potentials

$$\begin{aligned}V_S&=\alpha_S\rho_S+\beta_S\rho_S^2+\gamma_S\rho_S^3+\delta_S\Delta\rho_S\ ,\\V_V&=\alpha_V\rho_V+\gamma_V\rho_V^3+\delta_V\Delta\rho_V\ ,\end{aligned} \tag{16}$$

the isovector-scalar and isovector-vector potentials

$$\begin{aligned}V_{TS}&=\alpha_{TS}\rho_{TS}\ ,\\V_{TV}&=\alpha_{TV}\rho_{TV}\ ,\end{aligned} \tag{17}$$

and the Coulomb potential,

$$V_C=eA_0\ , \tag{18}$$

the Dirac equation can be written as

$$\begin{aligned}\{&i\boldsymbol\gamma\cdot\boldsymbol\partial+m+V_S+V_V\gamma_0+V_{TS}\tau_3+V_{TV}\tau_3\gamma_0\\&+V_C[(1-\tau_3)/2]\}u_k=\gamma_0\varepsilon_k u_k\ .\end{aligned} \tag{19}$$

For later use, we introduce the neutron and proton components of the scalar and vector densities and the scalar and vector potentials:

$$\begin{aligned}&\rho_S^n=\tfrac{1}{2}(\rho_S+\rho_{TS}),\quad \rho_S^p=\tfrac{1}{2}(\rho_S-\rho_{TS})\ ,\\&\rho_V^n=\tfrac{1}{2}(\rho_V+\rho_{TV}),\quad \rho_V^p=\tfrac{1}{2}(\rho_V-\rho_{TV})=j_0^p\ ,\\&V_S^n=V_S+V_{TS}\ ,\quad V_S^p=V_S-V_{TS}\ ,\ \text{and}\\&V_V^n=V_V+V_{TV},\quad V_V^p=V_V-V_{TV}\ .\end{aligned} \tag{20}$$

Note that a factor of $\frac{1}{2}$ appears for the densities, but not for the potentials.

The Hartree equations, Eqs. (19), are nonlinear equations because the potentials depend on the wave functions u_k. They are solved by iteration, that is, starting with some fixed potentials we solve Eqs. (19) as linear equations. From the wave functions obtained we calculate new potentials using Eqs. (10)–(11) and Eqs. (15)–(18). This procedure is repeated until suitable convergence criteria are satisfied. The convergence can be stabilized by introducing "damping," which means that the potential that is used in the next iteration is not the one calculated from the wave functions, but the average of the latter and the potential used when solving the previous iteration.

Because we consider only spherical closed major shell or closed subshell nuclei, we have only to deal with the radial equations. These ordinary differential equations are solved in configuration space by use of a shooting algorithm. We typically use a lattice with 300 points and a step size of $\frac{1}{20}$ fm. To accelerate the computation, we predict the initial single-particle energies from one iteration to the next in the shooting algorithm by use of perturbation theory.

C. Binding energy

The total energy E_T of the nuclear ground state is given by the integral of the ground state expectation value of the zero-zero component T_{00} of the energy-

momentum density tensor [14], namely,

$$E_T=\int d^3\mathbf{x}\{\langle\phi|T_{00}|\phi\rangle\} = \sum_{k=1}^{A}\varepsilon_k-\int d^3\mathbf{x}\{\langle\phi|\mathcal{L}|\phi\rangle\}\ , \tag{21}$$

where the first term is the sum over the single-particle energies of all occupied states and the second term is the volume integral of the ground state expectation value of the Lagrangian density given by Eqs. (1) and (2). Using the Dirac equation, Eq. (19), and the definitions, Eqs. (14) and (20), this equation becomes

$$E_T=\sum_{k=1}^{A}\varepsilon_k-\int d^3\mathbf{x}\{\tfrac{1}{2}\alpha_S\rho_S^2+\tfrac{1}{2}\alpha_V\rho_V^2+\tfrac{1}{2}\alpha_{TS}\rho_{TS}^2+\tfrac{1}{2}\alpha_{TV}\rho_{TV}^2+\tfrac{2}{3}\beta_S\rho_S^3+\tfrac{3}{4}\gamma_S\rho_S^4+\tfrac{3}{4}\gamma_V\rho_V^4+\tfrac{1}{2}\delta_S\rho_S\Delta\rho_S +\tfrac{1}{2}\delta_V\rho_V\Delta\rho_V+\tfrac{1}{2}j_0^p V_C\}\ . \tag{22}$$

The binding energy E_B of the nuclear ground state is given by the difference between the sum of the free (unbound) nucleon masses and E_T, with E_T corrected by the energy of the center-of-mass motion, $E_{\text{c.m.}}$:

$$E_B=Zm_p+Nm_n-(E_T-E_{\text{c.m.}})\ , \tag{23}$$

where $Z+N=A$, m_p is the free proton mass, and m_n is the free neutron mass. In this work we use an empirical expression for the $E_{\text{c.m.}}$ correction:

$$E_{\text{c.m.}}=(17.2\ \text{MeV})/A^{1/5}\ , \tag{24}$$

obtained by Reinhard [11] in a fit to spherical oscillator-basis calculations over the mass range $16\le A\le 208$. Within this range the magnitude of $E_{\text{c.m.}}$ satisfies the relation $9.9\ \text{MeV}\ge E_{\text{c.m.}}\ge 5.9\ \text{MeV}$. The empirical expression Eq. (24) reproduces [18] the exact calculations to within 5%.

D. Root-mean-square radii

The root-mean-square (rms) radii of the point neutron and point proton distributions, $\langle r^2\rangle_n^{1/2}$ and $\langle r^2\rangle_p^{1/2}$, are obtained from the second moments of the neutron and proton point densities. These point densities have already been expressed in terms of the isoscalar-vector and isovector-vector densities in Eq. (20). Using Eqs. (10), (14), and (20), we obtain

$$\langle r^2\rangle_n=\frac{1}{N}\int d^3\mathbf{x}\{x^2\rho_V^n(x)\} =\frac{1}{N}\int d^3\mathbf{x}\{x^2\tfrac{1}{2}[\rho_V(x)+\rho_{TV}(x)]\} =\frac{1}{N}\int d^3\mathbf{x}\left\{x^2\sum_i u_i^\dagger(x)u_i(x)\right\}\ , \tag{25}$$

where the index i ranges over all occupied neutron orbits. Similarly, we obtain

$$\langle r^2\rangle_p=\frac{1}{Z}\int d^3\mathbf{x}\{x^2\rho_V^p(x)\} =\frac{1}{Z}\int d^3\mathbf{x}\{x^2\tfrac{1}{2}[\rho_V(x)-\rho_{TV}(x)]\} =\frac{1}{Z}\int d^3\mathbf{x}\left\{x^2\sum_j u_j^\dagger(x)u_j(x)\right\}\ , \tag{26}$$

where the index j ranges over all occupied proton orbits. The root-mean-square radius of the charge distribution, $\langle r^2\rangle_{\text{charge}}^{1/2}$, is obtained by including finite nucleon size effects in the proton point density distribution that are due to the proton and neutron intrinsic charge distributions. Adopting the results of Friar and Negele [19] to our approach, we find

$$\langle r^2\rangle_{\text{charge}}=\langle r^2\rangle_p+\langle r_p^2\rangle+(N/Z)\langle r_n^2\rangle\ , \tag{27}$$

where $\langle r_p^2\rangle=0.6400\ \text{fm}^2$ and $\langle r_n^2\rangle=-0.1156\ \text{fm}^2$ are the mean-square charge radii of the proton and neutron, respectively. This expression is a good approximation [19] to the true mean-square charge radius, but a number of small corrections have been neglected. These include contributions from meson exchange currents and the center-of-mass motion correction, where the latter is increasingly important with decreasing mass number. For example, a harmonic oscillator model yields a -0.4% estimate for ^{208}Pb and a -15% estimate for ^{4}He, in the correction to the root-mean-square charge radius. We expect to include such corrections in future refinements of our model.

III. OPTIMIZATION OF COUPLING CONSTANTS

With the relativistic point coupling model described in Sec. II, the following ground state properties of spherical closed-shell nuclei can be calculated: (i) single-particle Dirac wave functions and energy levels (eigenvalues), (ii) point proton and point neutron densities and their moments, (iii) charge density and its moments, (iv) isoscalar-scalar, isoscalar-vector, isovector-scalar, and isovector-vector potentials (mean nucleon fields), and (v) binding energy (mass).

In order to calculate these quantities accurately, a physically realistic set of coupling constants must be determined. The test of a candidate set of coupling constants will be its predictive power in calculating these same quantities, as well as others, for nuclei other than those used in their determination. In this section we describe the general procedure for determining the coupling constants, the choice of nuclei to be used, and the choice of observables and their weights.

A. General procedure

The nine coupling constants to be determined for the relativistic point coupling model are listed in Table I. Four of these appear in the isoscalar-scalar potential V_S, three appear in the isoscalar-vector potential V_V, and one each appear in the isovector-scalar potential V_{TS} and the isovector-vector potential V_{TV}. The coupling constants appear explicitly in the time-independent Hartree equations of Dirac type, Eq. (13), and, equivalently, the potentials appear explicitly in the Dirac equations, Eq. (19).

As described in Sec. II B, we solve the nonlinear Dirac equations, Eq. (19), iteratively by starting with Woods-Saxon shapes and a fixed set of coupling constants for the initial solution and concluding, self-consistently, when predetermined convergence criteria have been met. This is the process for a given, fixed, set of coupling constants. To determine the *optimal* set of coupling constants, the Dirac equations solver, or, equivalently, Hartree equations solver is used as the function call in a generalized nonlinear least-squares minimization program [20] based on the Levenberg-Marquardt algorithm [21]. A flowchart for the entire process, shown in Fig. 1, facilitates a description of the procedure:

A set of nuclei $\{k\}$ is chosen that (a) satisfies the physical constraints implicit in Eqs. (13) and (19), and (b), possesses well-measured ground state observables $\{X^{(k)}_{\rm exp}\pm\Delta X^{(k)}_{\rm exp}\}$. For a given, fixed, set of coupling constants $\{p\}$ and, initially, Woods-Saxon shapes, the self-consistent solution to the Hartree equations is obtained and the corresponding theoretical values of the observables $\{X^{(k)}_{\rm th}(\{p\})\}$, depending on the set of coupling constants $\{p\}$, is computed. Then the generalized χ^2 is calculated,

$$\chi^2(\{p\})=\sum_{k\in\text{ nuclei}}\sum_{X\in\text{ observables}}\left[\frac{X^{(k)}_{\rm exp}-X^{(k)}_{\rm th}(\{p\})}{W^{(k)}_X X^{(k)}_{\rm exp}}\right]^2, \tag{28}$$

wherein the weights $W^{(k)}_X$ are given by

$$W^{(k)}_X=f^{(k)}_X\Delta X^{(k)}_{\rm exp}/X^{(k)}_{\rm exp}\ , \tag{29}$$

that is, the product of the external weight factor $f^{(k)}_X$ and the relative experimental uncertainty $\Delta X^{(k)}_{\rm exp}/X^{(k)}_{\rm exp}$ (ordinarily, $f^{(k)}_X=1.0$). The coupling constants $\{p\}$ are then adjusted by the Levenberg-Marquardt algorithm so as to reduce χ^2. The χ^2 computation/parameter adjustment/χ^2 reduction process is repeated until an (absolute) minimum in χ^2 is achieved. At this point, the final set of coupling constants $\{p_{\rm final}\}$ is tested by predicting the same observables, as well as others, for nuclei not included in the set $\{k\}$.

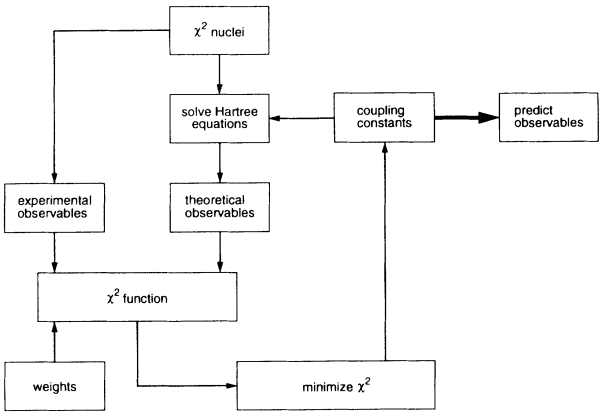

FIG. 1. Flowchart for application of the relativistic point coupling model.

We note here, for later use, the definitions of the generalized χ^2 per data point, $\chi^2_{N_{\rm obs}}$, where $N_{\rm obs}$ is the total number of measured observables contained in Eq. (28), and χ^2 per degree of freedom, $\chi^2_{\rm d.f.}$, where the number of degrees of freedom is $(N_{\rm obs}-N_p)$, with N_p the total number of parameters contained in Eq. (28):

$$\chi^2_{N_{\rm obs}}=\frac{1}{N_{\rm obs}}\chi^2(\{p\}) \tag{30}$$

and

$$\chi^2_{\rm d.f.}=\frac{1}{N_{\rm obs}-N_p}\chi^2(\{p\})\ . \tag{31}$$

B. Choice of nuclei

The physical constraints implied by Eqs. (13) and (19), which are correspondingly contained in our present computations, consist of the following: (1) The nucleus must be spherical and cannot be deformed. The total angular momentum of the nucleus must be zero. (2) The nuclear

TABLE I. Coupling constants of the relativistic point coupling model.

Potential	Coupling constant	Dimension	Description	
V_S	α_S	MeV^{-2}	isoscalar-scalar	linear
V_S	β_S	MeV^{-5}	isoscalar-scalar	quadratic
V_S	γ_S	MeV^{-8}	isoscalar-scalar	cubic
V_S	δ_S	MeV^{-4}	isoscalar-scalar	derivative
V_{TS}	α_{TS}	MeV^{-2}	isovector-scalar	linear
V_V	α_V	MeV^{-2}	isoscalar-vector	linear
V_V	γ_V	MeV^{-8}	isoscalar-vector	cubic
V_V	δ_V	MeV^{-4}	isoscalar-vector	derivative
V_{TV}	α_{TV}	MeV^{-2}	isovector-vector	linear

TABLE II. Sets of nuclei for the χ^2 optimization of the coupling constants.

Set A	Set B	Set C	Set D
^{4}He	. . .	. . .	. . .
^{16}O	^{16}O	^{16}O	^{16}O
^{40}Ca	^{40}Ca	^{40}Ca	. . .
^{48}Ca	^{48}Ca	^{48}Ca	. . .
^{56}Ni	^{56}Ni	^{56}Ni	. . .
. . .	. . .	^{88}Sr	^{88}Sr
^{90}Zr	^{90}Zr	. . .	. . .
. . .	. . .	^{114}Sn	. . .
^{132}Sn	^{132}Sn	^{132}Sn	. . .
. . .	. . .	^{140}Ce	. . .
. . .	. . .	^{146}Gd	. . .
^{208}Pb	^{208}Pb	^{208}Pb	^{208}Pb

orbit occupation probabilities must be either zero or one and the nucleus must be closed shell, or closed subshell, in both proton number and neutron number. This means that only even-even nuclei can be considered. Additionally, the set of nuclei chosen to determine the coupling constants of the model should have the following properties: (3) The nuclei should span wide ranges in mass number A, atomic number Z, and neutron-proton asymmetry $(N-Z)$. This provides for the possibilities of determining the sensitivities of the coupling constants to these parameters, and, correspondingly, of predicting nuclear properties over their wide ranges. (4) High-quality measurements of the ground-state observables for these nuclei should exist, in order that the χ^2 function has the least possible uncertainty.

Guided by the constraints (1)–(4), four sets of nuclei were chosen for the purpose of determining the coupling constants. These sets are labeled A, B, C, and D in Table II. Whereas the first of these sets contains all doubly magic nuclei, except for singly magic ^{90}Zr, each of the latter three sets span the same range in mass number, atomic number, and neutron-proton asymmetry, namely, 16–208, 8–82, and 0–44, respectively. There are twelve nuclear species in the table and seven of these are doubly magic, while the remaining five have one closed major shell (singly magic) and one closed minor shell. The magnitudes of the ground state quadrupole deformations ϵ_2 of the twelve species, determined in a fit [22] to experimental ground state masses, have an average absolute value $\overline{|\epsilon_2|}=0.006$ and satisfy the inequality $0.0\leq|\epsilon_2|\leq 0.017$. Thus, each nucleus chosen is either spherical or very close to spherical.

C. Choice of observables and weights

For each nucleus we selected the following four ground state observables: (1) the binding energy E_B, (2) the root-mean-square charge radius $\langle r^2\rangle^{1/2}_{\text{charge}}$, (3) the spin-orbit energy splitting for the least-bound neutron spin-orbit pair

$$\Delta E^{(n)}_{\text{s.o.}}=\varepsilon^{(n)}(n,l,j=l-\tfrac{1}{2})-\varepsilon^{(n)}(n,l,j=l+\tfrac{1}{2})\ , \tag{32}$$

and (4) the spin-orbit energy splitting for the least-bound proton spin-orbit pair

$$\Delta E^{(p)}_{\text{s.o.}}=\varepsilon^{(p)}(n,l,j=l-\tfrac{1}{2})-\varepsilon^{(p)}(n,l,j=l+\tfrac{1}{2})\ . \tag{33}$$

The first two of these observables depend sensitively upon the "nonrelativistic" combination of the scalar and vector mean nucleon fields, V_S+V_V. Alternatively, as a second-order reduction of the Dirac equation shows [23], the last two of these observables depend sensitively upon the "relativistic" combination of the scalar and vector fields, V_S-V_V. Thus, the observables have been chosen to provide sensitivities to both the sum and the difference of the scalar and vector mean fields. Note that in Eqs. (32) and (33) we have used the standard shell model notation, (nlj), for the principal, orbital angular momentum, and total angular momentum quantum numbers, respectively.

The binding energy (mass) is a most important observable, as it is sensitive to both the sum of the single-particle eigenvalues ε_k over all occupied orbitals and the total potential energy due to the mean nucleon fields [see Eqs. (22) and (23)]. In addition, the experimental masses are extremely well measured so they will dominate the magnitude of χ^2. For example, the average relative experimental uncertainty in the binding energy for the twelve nuclei of Table II is $1.2\times10^{-3}\%$. The root-mean-square charge radius is also a very important observable, as it is sensitive to the detail of the nuclear charge distribution and, therefore, to the point proton density, which itself depends sensitively on the single-particle wave functions $u_k(x)$, particularly their tail regions [see Eq. (26)]. The rms charge radii are also well measured in, e.g., electron scattering experiments, but usually not as well as the ground-state masses. The average relative experimental uncertainty in the rms charge radius for the eight nuclei of Table II that have been measured is $1.7\times10^{-1}\%$. [We use extrapolated values with large uncertainties (as large as 5%) for ^{56}Ni, ^{132}Sn, ^{140}Ce, and ^{146}Gd.]

The spin-orbit splittings for the least-bound neutron and proton spin-orbit pairs are not directly measurable and can only be inferred, usually from the single-hole states with respect to the nucleus of interest by pickup reactions. Moreover, the experimental single-hole state energies must be corrected for polarization effects, which are usually ignored, as they are expected to be small relative to the actual spin-orbit splitting [11]. We follow this practice and use the experimental single-hole state energies to construct the "experimental" spin-orbit splittings, for both neutrons and protons, in five of the eleven nuclei of Table II having spin-orbit splittings, namely, ^{16}O, ^{40}Ca, ^{48}Ca, ^{90}Zr, and ^{208}Pb. For the remaining six "unmeasured" nuclei we use the following approximation (for both neutrons and protons) due to Bohr and Mottelson [24]:

$$\Delta E^{(n)}_{\text{s.o.}}=\Delta E^{(p)}_{\text{s.o.}}\approx 10(2l+1)/A^{2/3}\ \text{MeV}\ . \tag{34}$$

This approximation is more accurate for larger values of the mass number A where individual variations are not as strong as for lighter nuclei. The smallest mass number

TABLE III. External weight factors $f_X^{(k)}$ and weights $W_X^{(k)}$ for set D.

Nucleus	f_{E_B}	$f_{\langle r^2\rangle^{1/2}_{\text{charge}}}$	$f_{\Delta E^{(n)}_{\text{s.o.}}}$	$f_{\Delta E^{(p)}_{\text{s.o.}}}$
^{16}O	100	1	1	1
^{88}Sr	100	1	1	1
^{208}Pb	100	1	1	1
Nucleus	W_{E_B}	$W_{\langle r^2\rangle^{1/2}_{\text{charge}}}$	$W_{\Delta E^{(n)}_{\text{s.o.}}}$	$W_{\Delta E^{(p)}_{\text{s.o.}}}$
^{16}O	0.0015	0.002	0.05	0.05
^{88}Sr	0.0015	0.002	0.50	0.50
^{208}Pb	0.0015	0.002	0.05	0.05

for which we use Eq. (34) is $A=56$. We use the following average relative "experimental" uncertainties for the neutron and proton spin-orbit splittings for the nuclei listed in Table II. In cases where single-hole states have been measured (^{16}O, ^{90}Zr, and ^{208}Pb) we use the value 5%. In cases where single-hole states have been measured but are fragmented (^{40}Ca and ^{48}Ca), we use the value 25%. If Eq. (34) is employed (^{56}Ni, ^{88}Sr, ^{114}Sn, ^{132}Sn, ^{140}Ce, and ^{146}Gd) we use the value 50%. In view of the magnitudes of these uncertainties, the total χ^2 will be influenced little by the spin-orbit energy splittings.

The sources of the experimental data that we use are the following. Measured masses and their uncertainties are taken from the midstream atomic mass evaluation of Audi [25], whereas measured rms charge radii and their uncertainties are taken from averages of model-independent analyses compiled by deVries and coworkers [26]. Single-hole state energies, and their uncertainties, for constructing spin-orbit splittings of the least-bound neutron and proton spin-orbit pairs, are taken from Refs. [24, 27–29].

In order to study the influence of the four observable types on the optimization of the coupling constants through the χ^2 minimization process, we have inserted an external weight factor $f_X^{(k)}$ in Eq. (29) for the weights $W_X^{(k)}$. As stated there, the ordinary value of $f_X^{(k)}$ is unity, otherwise $f_X^{(k)}>1.0$. A second reason for including the external weight factor is to take equal account of the physical influence of one observable type simultaneously with a second observable type that has been measured with enormously greater precision. Such a case exists in the present analysis, namely, the average relative experimental uncertainty in the binding energy is about two orders of magnitude smaller than the corresponding quantity for the rms charge radii (1.2×10^{-3}% vs 1.7×10^{-1}%). For this reason $f_{E_B}^{(k)}$ values of 10^2 will sometimes be used, whereas those for the remaining observable types will be set to unity.

To conclude this section, we present in Table III the final external weight factors $f_X^{(k)}$ and weights $W_X^{(k)}$ used in our analysis with set D of Table II, to be discussed in the next section.

IV. RESULTS

Our early studies considered sets A and B of Table II, which differ only by the presence or absence of ^{4}He, and examined convergence properties of the Hartree iterations under various model assumptions. Whereas a scalar-vector model of linear form with two coupling constants $\{\alpha_S\}$, $\{\alpha_V\}$ does not converge, one of linear, nonlinear, and derivative forms with six coupling constants $\{\alpha_S,\beta_S,\gamma_S,\delta_S\}$, $\{\alpha_V,\delta_V\}$ does converge for the eight nuclei with a *common* set of coupling constants. If the isoscalar-vector cubic term $\gamma_V\rho_V^3$ is included, for a total of seven terms, the measured observables are reproduced to within 10% except for ^{4}He where they are reproduced to within only 25%. Further study with sets A and B showed that deletion of ^{4}He yields an improvement in χ^2 per data point, $\chi^2_{N_{\text{obs}}}$, of a factor of 2.7. Two important studies were then performed with set B. The first was to test the importance of the derivative terms with coupling constants δ_S and δ_V. Here, a factor of 12.8 improvement in the χ^2 per degree of freedom, $\chi^2_{\text{d.f.}}$, was obtained in comparison with the same run, but with $\delta_S\equiv\delta_V\equiv0.0$. The second was to test the significance of introducing isospin through the isovector-scalar and isovector-vector linear terms, $\alpha_{TS}\rho_{TS}$ and $\alpha_{TV}\rho_{TV}$, respectively. Here, a factor of 17.6 improvement in $\chi^2_{\text{d.f.}}$ was obtained in comparison with the same run, but with $\alpha_{TS}\equiv\alpha_{TV}\equiv0.0$. At this point our model had become a scalar-vector model with both isoscalar and isovector components, represented by nine linear, nonlinear, and derivative terms with the corresponding nine coupling constants $\{\alpha_S,\beta_S,\gamma_S,\delta_S,\alpha_{TS}\}$, $\{\alpha_V,\gamma_V,\delta_V,\alpha_{TV}\}$. This model was tested using set C of Table II to (a) again demonstrate convergence in the Hartree iterations with a common set of coupling constants, and (b) demonstrate that the convergence is independent of the set of nuclei chosen from Table II. Both of these requirements were met satisfactorily.

We then commenced a search for the optimal set of nine coupling constants, using set C of Table II, in a series of systematic searches. The results were somewhat disappointing in the sense that while several minima in $\chi^2_{N_{\text{obs}}}$ were found, it was not clear which of the corresponding sets of coupling constants are the most physical, that is, have the most predictive power. This is because these particular sets have almost equivalent predictive powers, with similar values for all coupling constants except those of the isovector terms, α_{TS} and α_{TV}, and sometimes that of the isoscalar-vector cubic term γ_V. This situation led us to reexamine the properties of the nuclei in sets A–C in terms of the constraints given in Sec. III B, especially that of orbital occupation numbers of only 0 or 1. A more stringent review of these constraints led us to construct set D of Table II wherein ^{16}O and ^{208}Pb are perhaps the two nuclei that best satisfy them and ^{88}Sr, of intermediate mass, may be the best choice among the remaining eight nuclei of set C. [Note that the nuclei of set D span the same mass number, atomic number, and neutron-proton asymmetry ranges as sets B and C.] We then tested our model using set D and found a minimum in $\chi^2_{N_{\text{obs}}}$ with a corresponding set of coupling constants that are very similar to a subset of those found with set C except for the value of the isovector-scalar coupling constant α_{TS}. As will be seen in the next subsections, the contribution of the isovector-

scalar term to the total potential is very small, which is probably the reason why it is so difficult to precisely determine the value of its coupling constant α_{TS}. The coupling constants determined with set D have the most predictive power to date for this model and they will be used throughout the remainder of this paper.

A. Coupling constants

The optimal set of the nine coupling constants of our model, determined using set D of Table II, is given in Table IV. The first four of these are associated with the isoscalar-scalar potential V_S given by Eq. (16). The fifth is associated with the isovector-scalar potential V_{TS} given by Eq. (17). The sixth through eighth are associated with the isoscalar-vector potential V_V, also given by Eq. (16), and the ninth is associated with the isovector-vector potential V_{TV}, also given by Eq. (17). Except for the coupling constants of the derivative terms, δ_S and δ_V, a positive coupling constant corresponds to a repulsive term in the potential and a negative coupling constant corresponds to an attractive term in the potential. The derivative terms generally contain both repulsive and attractive regions depending usually upon whether one is considering the interior or surface regions of the nucleus. The dimensions of the coupling constants are determined by recalling that for units in which $\hbar=c=1$, a length has a dimension of inverse energy. We note here that the ratio of isovector-scalar to isovector-vector coupling constants is indeed small, $\alpha_{TS}/\alpha_{TV} = 7.402\,91\times10^{-7}/3.256\,77\times10^{-5} \approx 0.023$. Furthermore, the ratio of isovector-scalar to isoscalar-scalar coupling constants is even smaller, $\alpha_{TS}/\alpha_S = -7.402\,91\times10^{-7}/4.507\,65\times10^{-4} \approx -0.0016$. Thus, the influence of the isovector-scalar term on the total potential will be very small, so the fact that we have not precisely determined its value should have little effect on our calculated results. It is not surprising that the isovector-scalar term is small because it corresponds to an isovector-scalar meson field for the exchange of the δ meson. The one-boson exchange contribution of the δ meson goes as g_δ^2/m_δ^2, but the mass of the δ meson is relatively large, $m_\delta=983$ MeV, and the coupling constant is relatively small, $g_\delta\sim2$, so its contribution is small [30].

TABLE IV. Optimized coupling constants for the relativistic point coupling model.

Potential	Coupling constant	Magnitude	Dimension
V_S	α_S	$-4.507\,65\times10^{-4}$	MeV^{-2}
V_S	β_S	$1.109\,51\times10^{-11}$	MeV^{-5}
V_S	γ_S	$5.735\,22\times10^{-17}$	MeV^{-8}
V_S	δ_S	$-4.239\,44\times10^{-10}$	MeV^{-4}
V_{TS}	α_{TS}	$7.402\,91\times10^{-7}$	MeV^{-2}
V_V	α_V	$3.426\,65\times10^{-4}$	MeV^{-2}
V_V	γ_V	$-4.388\,58\times10^{-17}$	MeV^{-8}
V_V	δ_V	$-1.143\,65\times10^{-10}$	MeV^{-4}
V_{TV}	α_{TV}	$3.256\,77\times10^{-5}$	MeV^{-2}

B. Observables

A comparison of calculated and measured observables for the nuclei of set D is given in Table V. The agreement is quite good, as one expects, because the measured observables were used in the minimization of χ^2 to optimize the coupling constants. An inspection of the table shows that relative errors with respect to measured binding energies range from 0.08% to 0.19%, that relative errors with respect to measured root-mean-square charge radii range from 0.16% to 0.62%, and that relative errors with respect to measured spin-orbit splittings range from 0.49 to 47.6%. The roughly comparable relative errors in the calculated binding energies and root-mean-square charge radii reflect our intent to obtain comparable influence from these two important observables in determining the coupling constants (see Table III and discussion). Note that the 47.6% relative error for the $1d_{3/2}$-$1d_{5/2}$ proton spin-orbit splitting in ^{208}Pb is anomalously large with respect to those for the other three measured spin-orbit splittings, particularly that of the $2p_{1/2}$-$2p_{3/2}$ neutron spin-orbit splitting in the same nucleus with a value of 1.56%. We have no explanation as to why the neutron spin-orbit splitting is reproduced so well in ^{208}Pb while that for the proton is reproduced so poorly. The same problem occurs for other nonrelativistic [27] and relativistic [3] Hartree calculations for ^{208}Pb.

More generally, the comparison between calculated and measured single-particle energies for the nuclei of set D is as good, or better, than other similar calculations of which we are aware [1–3,6–8,10,11]. Table VI gives a comparison with experiment for ^{16}O and ^{208}Pb as evidence for this point. We note two additional points with respect to this table: (a) the calculated $1f_{5/2}$ and $2p_{3/2}$ neutron levels in ^{208}Pb are inverted in comparison with experiment, and this inversion is common to many other theoretical calculations, both nonrelativistic and relativistic, and (b) unlike the work of Horowitz and Serot [3] and Serot and Walecka [6], we do not obtain an inversion of the calculated $0g_{9/2}$ and $1p_{1/2}$ proton levels, in contrast to experiment. However, although we have the ordering of the latter two levels correct, they are nevertheless too

TABLE V. Comparison of calculated and measured observables for the nuclei used to optimize the coupling constants.

Nucleus		E_B (MeV)	$\langle r^2\rangle^{1/2}_{\mathrm{charge}}$ (fm)	$\Delta E^{(n)}_{\mathrm{s.o.}}$ (MeV)	$\Delta E^{(p)}_{\mathrm{s.o.}}$ (MeV)
^{16}O	Calc.	127.44	2.732	6.385	6.355
	Exp.	127.62	2.737	6.176	6.324
	Diff.	−0.18	−0.005	0.209	0.031
^{88}Sr	Calc.	769.92	4.214	1.939	6.116
	Exp.	768.47	4.188	1.516[a]	3.538[a]
	Diff.	1.45	0.026	0.423	2.578
^{208}Pb	Calc.	1635.10	5.511	0.912	1.963
	Exp.	1636.47	5.502	0.898	1.332
	Diff.	−1.37	0.009	0.014	0.631

[a]Calculated using Eq. (34).

TABLE VI. Comparison of calculated and measured single-particle energies for ^{16}O and ^{208}Pb.

Neutrons			Protons		
S.P. level	Calc. (MeV)	Exp. (MeV)	S.P. level	Calc. (MeV)	Exp. (MeV)
		A. ^{16}O			
$0p_{1/2}$	−15.355	−15.664	$0p_{1/2}$	−11.512	−12.128
$0p_{3/2}$	−21.740	−21.840	$0p_{3/2}$	−17.868	−18.451
$0s_{1/2}$	−41.413	−47±7	$0s_{1/2}$	−37.270	−40±8
		B. ^{208}Pb			
$2p_{1/2}$	−6.818	−7.368	$2s_{1/2}$	−8.191	−8.013
$1f_{5/2}$	−8.489	−7.938	$1d_{3/2}$	−9.435	−8.364
$2p_{3/2}$	−7.730	−8.266	$0h_{11/2}$	−10.604	−9.361
$0i_{13/2}$	−9.791	−9.001	$1d_{5/2}$	−11.397	−9.696
$1f_{7/2}$	−11.051	−9.708	$0g_{7/2}$	−15.747	−11.487
$0h_{9/2}$	−13.732	−10.781	$0g_{9/2}$	−19.906	−15.413
$2s_{1/2}$	−18.236	...	$1p_{1/2}$	−20.475	...
$1d_{3/2}$	−19.133	...	$1p_{3/2}$	−21.619	...

deeply bound, in common with other relativistic mean field approaches [3,7,12].

We turn now to a discussion of the densities and corresponding potentials that were used to obtain the calculated observables that have just been discussed.

C. Densities

We show the isoscalar-scalar densities, ρ_s, the isoscalar-vector densities, ρ_V, the isovector-scalar densities, ρ_{TS}, and the isovector-vector densities, ρ_{TV}, for the nuclei of set D in Figs. 2–5. These densities, shown here for the nuclei used to determine the coupling constants of Table IV, are defined by Eqs. (10) and (14). The gross structure of the isoscalar densities is as one would expect: Woods-Saxon-like shapes with similar surface diffuseness properties (logarithmic plots show very similar slopes in the surface regions), and central densities of approximately 0.15 fm^{-3}. A closer examination shows that the surface diffuseness properties of isoscalar-scalar and isoscalar-vector densities are also very similar and that the central regions of the isoscalar-vector (baryon) densities are slightly larger, about 0.01 fm^{-3}, than the corresponding central regions of the isoscalar-scalar densities.

The structure in the interiors of the isoscalar densities is due to the orbital contributions of the single-particle wave functions [see Eqs. (10)]. For ^{16}O one observes a minimum at the origin and a maximum just beyond 1 fm, for ^{88}Sr there are two minima and two maxima, and for ^{208}Pb there are one minima and two maxima.

The isovector densities, Figs. 4 and 5, exhibit much more structure than the isoscalar densities. This is because these densities are equal to the differences between the neutron and proton components of the isoscalar densities. From Eqs. (20) one has

$$\rho_{TS}=\rho_S^n-\rho_S^p$$

and (35)

$$\rho_{TV}=p_V^n-\rho_V^p\ .$$

Accordingly, the isovector densities are sensitive to the

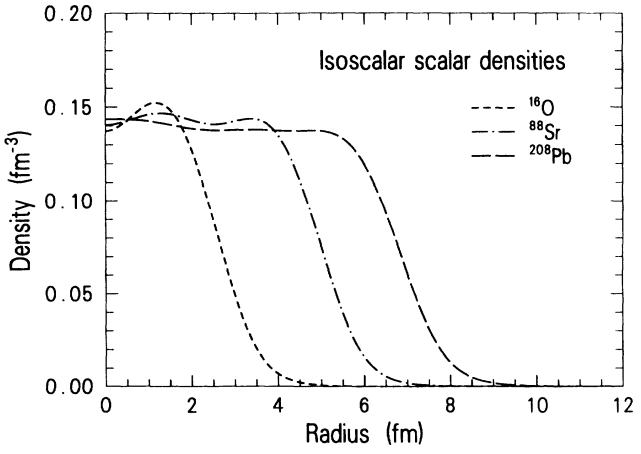

FIG. 2. Isoscalar-scalar densities $\rho_S(r)$ for the nuclei used to optimize the coupling constants.

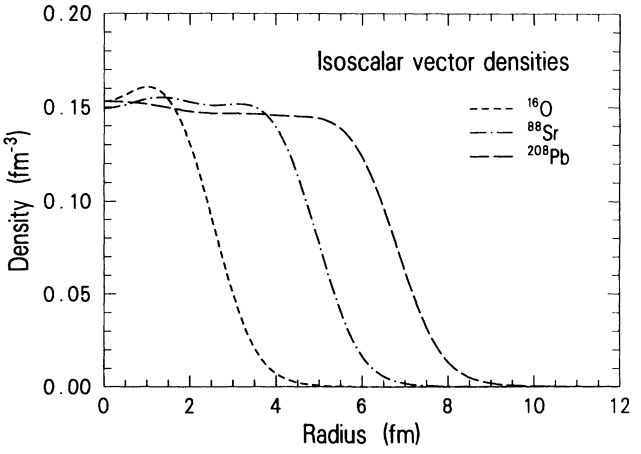

FIG. 3. Isoscalar-vector densities $\rho_V(r)$, or baryon densities, for the nuclei used to optimize the coupling constants.

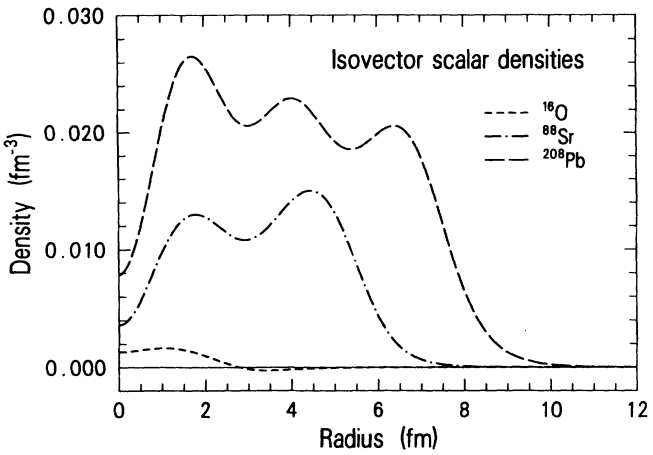

FIG. 4. Isovector-scalar densities $\rho_{TS}(r)$ for the nuclei used to optimize the coupling constants.

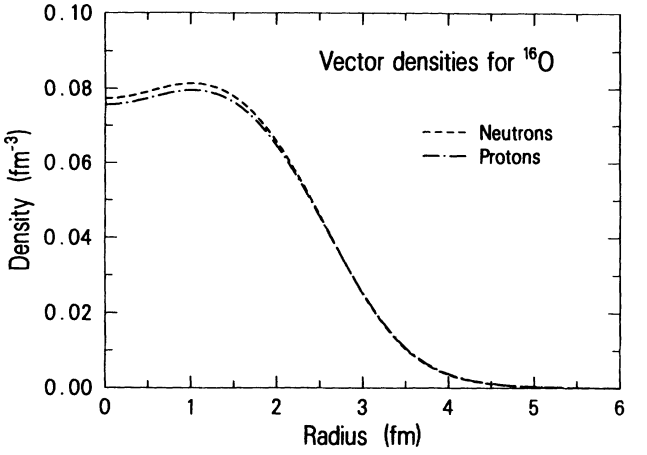

FIG. 6. Neutron and proton point densities $\rho_V^n(r)$ and $\rho_V^p(r)$, respectively, for ^{16}O. Their sum is the isoscalar-vector (baryon) density for ^{16}O shown in Fig. 3.

differences between the orbital contributions of the single-particle neutron wave functions and the single-particle proton wave functions. For ^{208}Pb there are three distinct maxima and minima and for ^{88}Sr there are two each. For the $N=Z$ nucleus ^{16}O, one observes that the protons are shifted somewhat to the outside [the isovector-vector density of Fig. 5 becomes negative at $r=2.86$ fm] due presumably to Coulomb repulsion.

The point neutron and point proton densities ρ_V^n and ρ_V^p, respectively, are the neutron and proton components of the isoscalar-vector (baryon) densities ρ_V shown in Fig. 3. The point densities for these three nuclei are shown in Figs. 6–8. In ^{16}O, Fig. 6, the neutron point density is somewhat larger in the interior whereas the proton point density just exceeds the neutron point density in the surface region, in agreement with Fig. 5. For ^{88}Sr, shown in Fig. 7 with a neutron excess $N-Z=38$, the point neutron density exceeds the point proton density over the entire nucleus. The same is true for ^{208}Pb, shown in Fig. 8, with a neutron excess $N-Z=44$. Here it is interesting to note that whereas the point neutron density has a minimum at the origin, the point proton density has a maximum at the origin, in agreement with the findings of

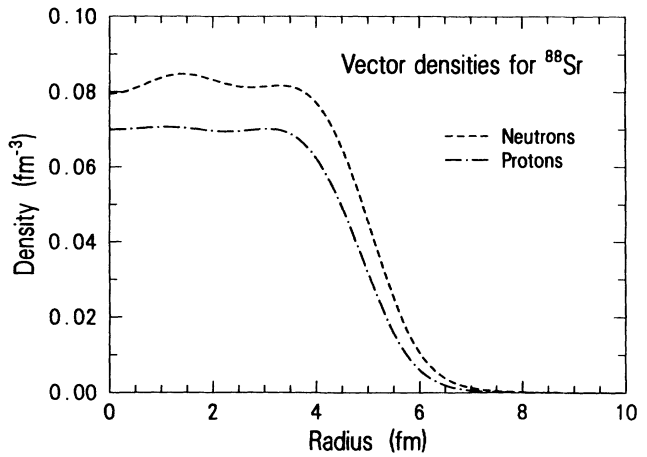

FIG. 7. Neutron and proton point densities $\rho_V^n(r)$ and $\rho_V^p(r)$, respectively, for ^{88}Sr. Their sum is the isoscalar-vector (baryon) density for ^{88}Sr shown in Fig. 3.

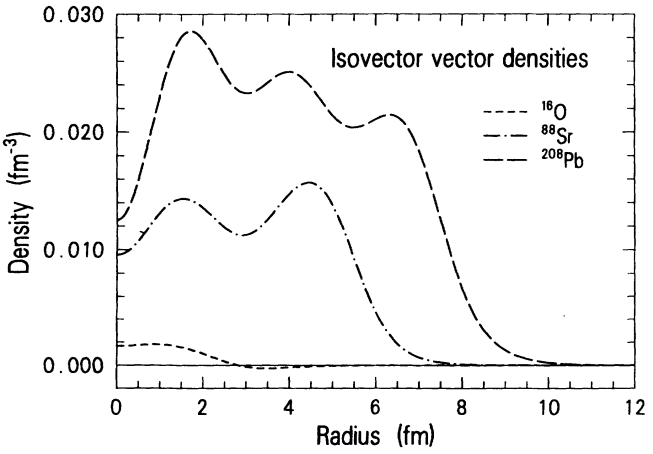

FIG. 5. Isovector-vector densities $\rho_{TV}(r)$ for the nuclei used to optimize the coupling constants.

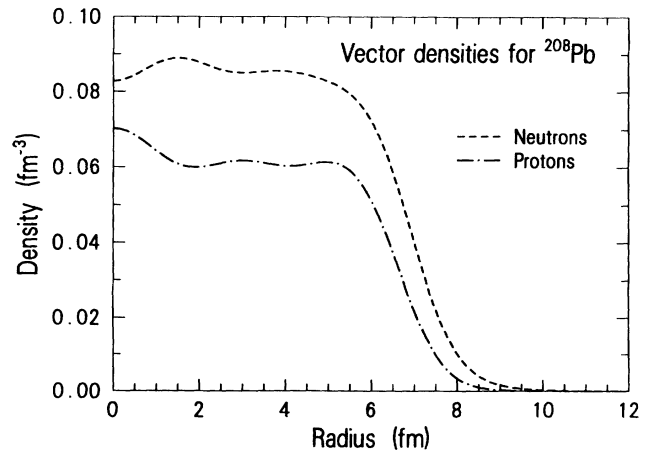

FIG. 8. Neutron and proton point densities $\rho_V^n(r)$ and $\rho_V^p(r)$, respectively, for ^{208}Pb. Their sum is the isoscalar-vector (baryon) density for ^{208}Pb shown in Fig. 3.

TABLE VII. Calculated root-mean-square radii of the point neutron and point proton densities for the nuclei used to optimize the coupling constants.

Nucleus	$\langle r^2\rangle_n^{1/2}$ (fm)	$\langle r^2\rangle_p^{1/2}$ (fm)
^{16}O	2.608	2.634
^{88}Sr	4.308	4.156
^{208}Pb	5.721	5.469

Horowitz and Serot [3]. Another way of assessing the point neutron and point proton densities is to calculate their second moments, the mean-square radii. The root-mean-square radii for the point densities shown in Figs. 6–8, calculated using Eqs. (25) and (26), are given in Table VII. Inspection of this table yields a measure as to the extent the protons in ^{16}O are outside of the neutrons, and as to the extent the neutrons in ^{88}Sr and ^{208}Pb are outside of the respective protons. Namely, for ^{16}O, $\langle r^2\rangle_p^{1/2}-\langle r^2\rangle_n^{1/2}$ has the value 0.026 fm, and for ^{88}Sr and ^{208}Pb, $\langle r^2\rangle_n^{1/2}-\langle r^2\rangle_p^{1/2}$ has the values 0.152 fm and 0.252 fm, respectively.

D. Potentials

Corresponding to the densities shown in the previous subsection, we show here the isoscalar-scalar potentials V_S, the isoscalar-vector potentials V_V, the isovector-scalar potentials V_{TS}, and the isovector-vector potentials V_{TV}, for the nuclei of set D in Figs. 9–11. These potentials, constructed from the coupling constants of Table IV and the densities just discussed, are defined by Eqs. (16) and (17). Similar to the gross structure of the isoscalar densities, the isoscalar potentials have Woods-Saxon-like shapes with similar surface diffuseness properties for the three nuclei of set D. The central strengths of the isoscalar-scalar potentials, V_S, are approximately -400 MeV, while those of the isoscalar-vector potentials V_V, are approximately $+325$ MeV. Inspection of Fig. 9 reveals that the scalar potentials are longer ranged than the corresponding vector potentials, in agreement with ex-

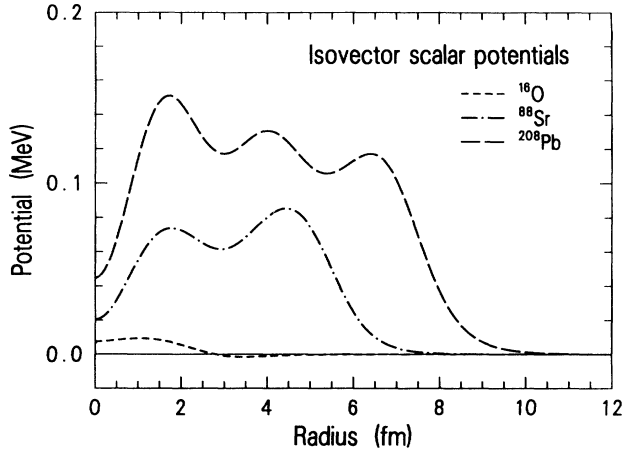

FIG. 10. Isovector-scalar potentials $V_{TS}(r)$ for the nuclei used to optimize the coupling constants.

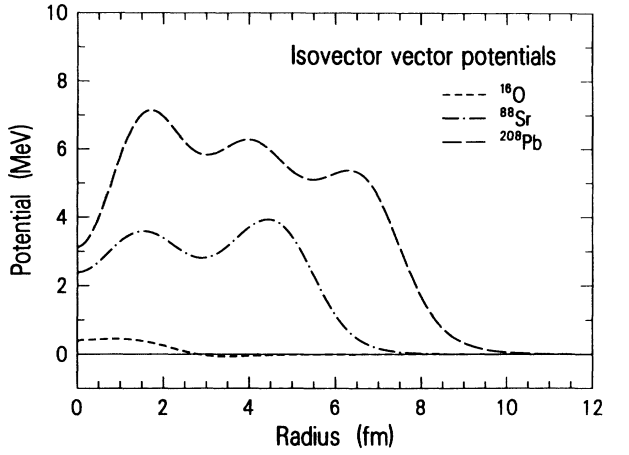

FIG. 11. Isovector-vector potentials $V_{TV}(r)$ for the nuclei used to optimize the coupling constants.

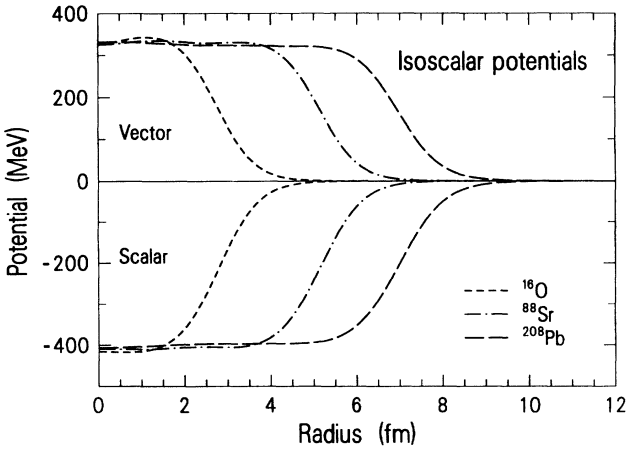

FIG. 9. Isoscalar-scalar and isoscalar-vector potentials $V_S(r)$ and $V_V(r)$, respectively, for the nuclei used to optimize the coupling constants.

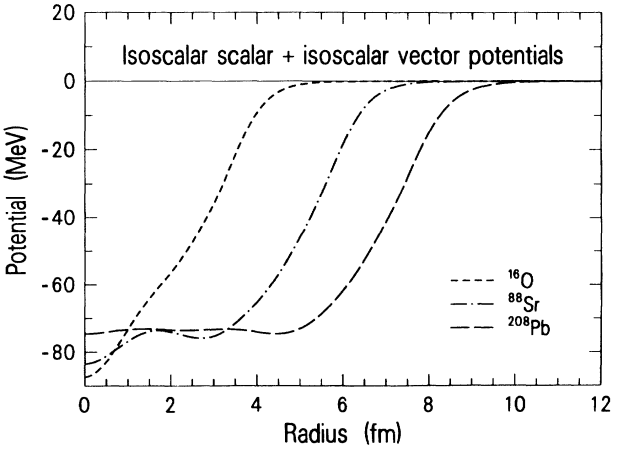

FIG. 12. Sum of the isoscalar-scalar and isoscalar-vector potentials $V_S(r)$ and $V_V(r)$, respectively, for the nuclei used to optimize the coupling constants.

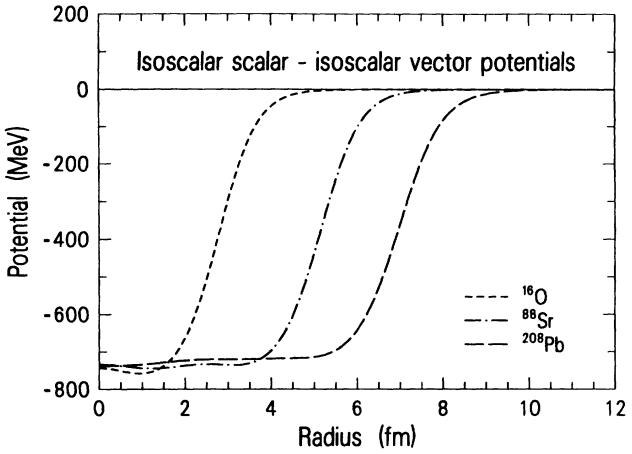

FIG. 13. Difference of the isoscalar-scalar and isoscalar-vector potentials $V_S(r)$ and $V_V(r)$, respectively, for the nuclei used to optimize the coupling constants.

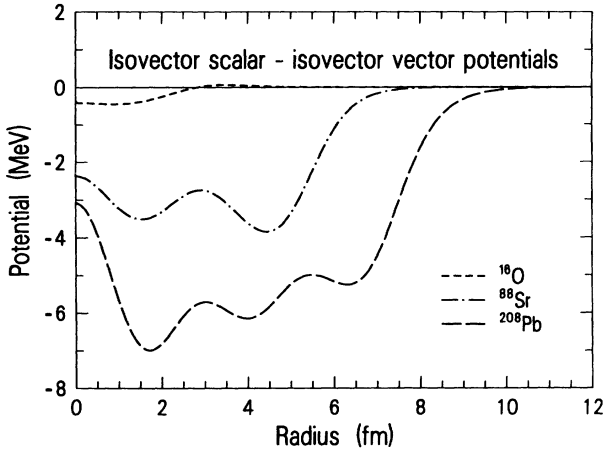

FIG. 15. Difference of the isovector-scalar and isovector-vector potentials $V_{TS}(r)$ and $V_{TV}(r)$, respectively, for the nuclei used to optimize the coupling constants.

pectations based upon the static potential limit for a one-boson-exchange potential (OBEP) from scalar (σ) and vector (ω) meson exchange [6]. Finally, a comparison of Fig. 9 with Figs. 2 and 3 shows that the isoscalar potentials have less structure in the interior regions than do the corresponding isoscalar densities. This is due to the smoothing that is produced by the nonlinear and derivative terms appearing in the isoscalar potentials.

The isovector potentials V_{TS} and V_{TV} are shown in Figs. 10 and 11, respectively. As these potentials are linear in the corresponding isovector densities ρ_{TS} and ρ_{TV} [see Eq. (17)], their shapes are the same as those of Figs. 4 and 5. Figures 9–11 show that the isovector-scalar, isovector-vector, and isoscalar potential strengths are in the approximate ratio 0.1 MeV/5 MeV/400 MeV. The physical significance of the isovector-scalar and isovector-vector potentials is the same as for the corresponding isovector densities, namely, sensitivity to the *differences* between orbital contributions of the single-particle neutron wave functions and the single-particle proton wave functions. Analogous to Eq. (35), one finds from Eq. (20) that

$$V_{TS}=\tfrac{1}{2}(V_S^n-V_S^p)$$

and (36)

$$V_{TV}=\tfrac{1}{2}(V_V^n-V_V^p)\ ,$$

with corresponding physical interpretations.

The sums and differences of the isoscalar-scalar and isoscalar-vector potentials V_S and V_V are shown in Figs. 12 and 13 for the nuclei of set D. The same is shown in Figs. 14 and 15 for the isovector-scalar and isovector-vector potentials V_{TS} and V_{TV}. In the nonrelativistic limit ($m_n, m_p \to \infty$) the Dirac equation is equivalent to a Schrödinger equation with a central potential $V_{\rm cen}^{\rm nr}=V_S+V_V$ and a spin-orbit potential, of Thomas form, constructed from $V_{\rm s.o.}^{\rm nr}=V_S-V_V$. More accurately,

$$V_{\rm cen}^{\rm nr}({\rm neutron})=V_S^n+V_V^n$$
$$=(V_S+V_V)+(V_{TS}+V_{TV})\ , \quad (37)$$

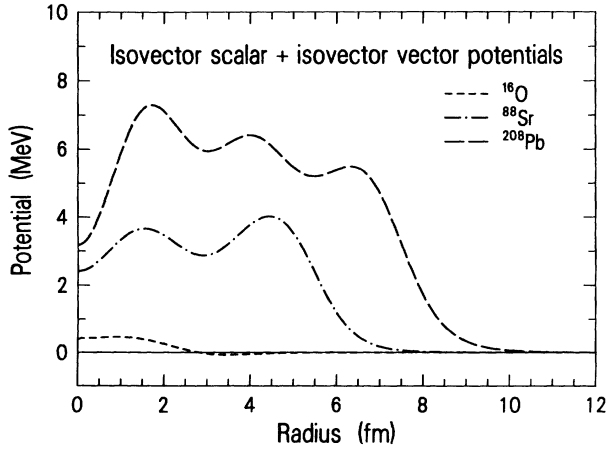

FIG. 14. Sum of the isovector-scalar and isovector-vector potentials $V_{TS}(r)$ and $V_{TV}(r)$, respectively, for the nuclei used to optimize the coupling constants.

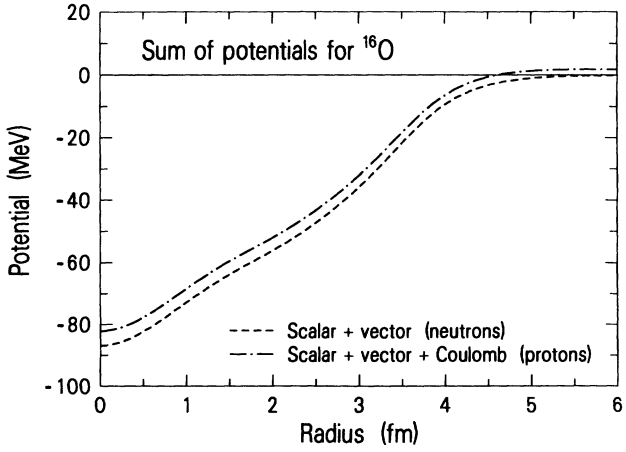

FIG. 16. Neutron and proton potentials $V_S^n(r)+V_V^n(r)$ and $V_S^p(r)+V_V^p(r)+V_C(r)$, respectively, for ^{16}O.

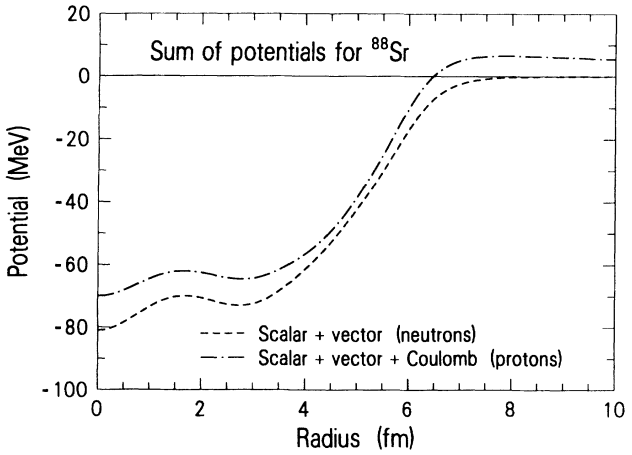

FIG. 17. Neutron and proton potentials $V_S^n(r)+V_V^n(r)$ and $V_S^p(r)+V_V^p(r)+V_C(r)$, respectively, for ^{88}Sr.

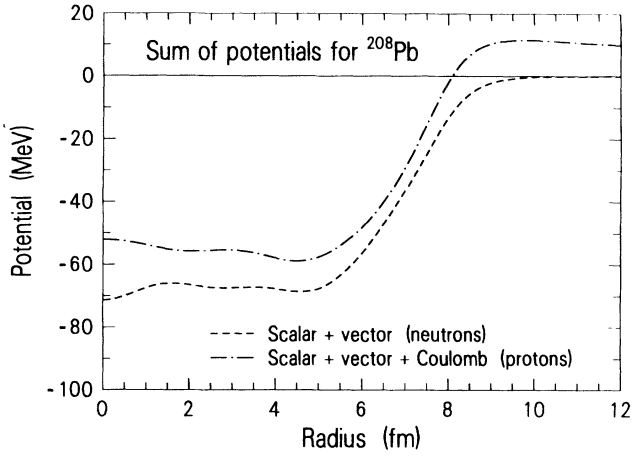

FIG. 18. Neutron and proton potentials $V_S^n(r)+V_V^n(r)$ and $V_S^p(r)+V_V^p(r)+V_C(r)$, respectively, for ^{208}Pb.

$$V_{\text{cen}}^{\text{nr}}(\text{proton})=V_S^p+V_V^p+V_C$$
$$=(V_S+V_V)-(V_{TS}+V_{TV})+V_C\ , \tag{38}$$
$$V_{\text{s.o.}}^{\text{nr}}(\text{neutron})=V_S^n-V_V^n$$
$$=(V_S-V_V)+(V_{TS}-V_{TV})\ , \text{ and} \tag{39}$$
$$V_{\text{s.o.}}^{\text{nr}}(\text{proton})=V_S^p-V_V^p-V_C$$
$$=(V_S-V_V)-(V_{TS}-V_{TV})-V_C\ . \tag{40}$$

Thus, the nonrelativistic combinations appearing in the Schrödinger central neutron potentials for the nuclei of set D are given by the *sums* of corresponding curves in Figs. 12 and 14, whereas those combinations appearing in the Schrödinger central proton potentials are given by the *differences* of corresponding curves in Figs. 12 and 14, plus the Coulomb potential. Similarly, the nonrelativistic combinations appearing in the Schrödinger spin-orbit potential of Thomas form for neutrons are given by the *sums* of corresponding curves in Figs. 13 and 15, whereas these combinations appearing in the Schrödinger spin-orbit potential of Thomas form for protons are given by the *differences* of corresponding curves in Figs. 13 and 15, minus the Coulomb potential.

We show the Schrödinger-equivalent nonrelativistic central neutron and proton potentials, Eqs. (37) and (38), for the nuclei of set D in Figs. 16–18. For these nuclei, the proton potentials range from ~ -50 MeV to ~ -80 MeV in depth, from ^{208}Pb to ^{16}O, whereas the corresponding neutron potentials range from ~ -70 MeV to ~ -90 MeV in depth. Clearly, the potentials for ^{16}O, Fig. 16, do not have Woods-Saxon forms, whereas those for ^{208}Pb, Fig. 18, could at least be approximated by Woods-Saxon forms. It is interesting to note from Table VI that the $0s_{1/2}$ neutron and proton levels for ^{16}O are at -41.413 and -37.270 MeV, respectively, and that for ^{208}Pb the corresponding $0s_{1/2}$ levels [not included in Table VI] are at -60.726 and -50.228 MeV. Thus, in ^{16}O the bottoms of the wells are ~ 45 MeV below the lowest single-particle levels and in ^{208}Pb the bottom of the neutron well is ~ 3 MeV below the lowest single-particle neutron level and the bottom of the proton well is ~ 11 MeV below the lowest single-particle proton level.

We do not show the non-relativistic spin-orbit combinations, Eqs. (39) and (40), appearing in the Schrödinger spin-orbit potentials of Thomas form because they are only very slightly different from the curves shown for V_S-V_V in Fig. 13. That is, Eqs. (39) and (40) are overwhelmingly dominated by their first terms. The central magnitudes of V_S-V_V, approximately -725 MeV, together with the magnitudes of their gradients $|\nabla(V_S-V_V)|$, appear necessary to explain the large nuclear spin-orbit splittings that are experimentally observed.

V. PREDICTIONS OF NUCLEAR GROUND STATE PROPERTIES AND NUCLEAR MATTER

In this section we test our relativistic point coupling model by comparing predicted and measured observables. For this purpose we use the fixed set of nine optimized coupling constants determined in Sec. IV and listed in Table IV. None of the nuclei of set D, used to determine the optimized coupling constants, is considered in this section. At the end of the section we predict nuclear matter properties with a subset of the coupling constants of Table IV.

A. Choice of nuclei

As discussed in Sec. III B, the current status of our model and corresponding computer code constrains the test nuclei to be (a) spherical nuclei with ground state total angular momentum $\mathbf{J}_{\text{g.s.}}=0$, and (b) even-even closed-shell nuclei or closed-subshell nuclei in both proton number Z and neutron number N. We satisfied both (a) and (b) by forming the intersection of two sets of nuclei:

Set 1 = {even-even nuclei with $J_{g.s.}=0$ and with ground state quadrupole deformations $|\epsilon_2| \leq 0.05$} , and

Set 2 = nuclei with $Z \in \{2,6,8,14,16,20,28,32,38,40,50,58,64,76,80,82\}$

and with $N \in \{2,6,8,14,16,20,28,32,38,40,50,56,64,66,70,82,90,100,114,118,124,126\}$.

TABLE VIII. Comparison of predicted and measured observables.

Nucleus		E_B (MeV)	$\langle r^2 \rangle^{1/2}_{\text{charge}}$ (fm)	Neutron shell	$\Delta E^{(n)}_{\text{s.o.}}$ (MeV)	Proton shell	$\Delta E^{(p)}_{\text{s.o.}}$ (MeV)
^{4}He	Calc.	27.77	2.137	. . .	. . .	. . .	. . .
	Expt.	28.30	1.681				
	Diff.	−0.53	0.456				
^{8}He	Calc.	33.76	2.010	. . .	. . .	. . .	. . .
	Exp.	31.41	2.467[a]				
	Diff.	2.35	−0.457				
^{10}He	Calc.	33.98	2.031	0*p*	3.994	. . .	. . .
	Exp.	. . .	. . .		. . .		
	Diff.	. . .	. . .		. . .		
^{8}C	Calc.	26.06	3.039	. . .	. . .	. . .	. . .
	Exp.	24.78	. . .				
	Diff.	1.28	. . .				
^{14}C	Calc.	104.63	2.568	0*p*	6.571	. . .	. . .
	Exp.	105.29	2.56		. . .		
	Diff.	−0.66	0.008		. . .		
^{20}C	Calc.	116.38	2.595	0*p*	5.503	. . .	. . .
	Exp.	119.14	. . .		. . .		
	Diff.	−2.76	. . .		. . .		
^{22}C	Calc.	120.52	2.608	0*p*	5.609	. . .	. . .
	Exp.	120.34	. . .		. . .		
	Diff.	0.18	. . .		. . .		
^{14}O	Calc.	97.82	2.763	. . .	. . .	0*p*	6.447
	Exp.	98.73	. . .				. . .
	Diff.	−0.91	. . .				. . .
^{22}O	Calc.	162.70	2.730	0*p*	5.247	0*p*	5.524
	Exp.	161.87	. . .		. . .		. . .
	Diff.	0.83	. . .		. . .		. . .
^{24}O	Calc.	170.19	2.742	0*p*	5.577	0*p*	5.730
	Exp.	168.81	. . .		. . .		. . .
	Diff.	1.38	. . .		. . .		. . .
^{28}O	Calc.	176.41	2.814	0*d*	6.202	0*p*	4.771
	Exp.	165.91[b]	. . .		. . .		. . .
	Diff.	10.50	. . .		. . .		. . .
^{20}Si	Calc.	83.24	3.374	. . .	. . .	0*p*	5.386
	Exp.	. . .	. . .				. . .
	Diff.	. . .	. . .				. . .
^{22}Si	Calc.	135.25	3.215	0*p*	5.423	0*p*	5.185
	Exp.	134.30	. . .		. . .		. . .
	Diff.	0.95	. . .		. . .		. . .

TABLE VIII. (*Continued*).

Nucleus		E_B (MeV)	$\langle r^2 \rangle^{1/2}_{\text{charge}}$ (fm)	Neutron shell	$\Delta E^{(n)}_{\text{s.o.}}$ (MeV)	Proton shell	$\Delta E^{(p)}_{\text{s.o.}}$ (MeV)
^{34}Si	Calc.	284.14	3.178	0*d*	7.176	0*p*	4.066
	Exp.	283.43	· · ·		· · ·		· · ·
	Diff.	0.71	· · ·		· · ·		· · ·
^{36}S	Calc.	305.84	3.285	0*d*	7.234	0*p*	4.552
	Exp.	308.72	3.278		· · ·		· · ·
	Diff.	−2.88	0.007		· · ·		· · ·
^{34}Ca	Calc.	245.20	3.469	0*p*	3.952	0*d*	6.961
	Exp.	244.84[b]	· · ·		· · ·		· · ·
	Diff.	0.36	· · ·		· · ·		· · ·
^{40}Ca	Calc.	343.16	3.451	0*d*	6.848	0*d*	6.844
	Exp.	342.05	3.465		6.3		7.2
	Diff.	1.11	−0.014		0.548		−0.356
^{48}Ca	Calc.	417.13	3.479	0*d*	5.874	0*d*	6.138
	Exp.	415.99	3.451		3.6		4.3
	Diff.	1.14	0.028		2.274		1.838
^{52}Ca	Calc.	435.08	3.503	0*d*	6.000	0*d*	6.133
	Exp.	436.53	· · ·		· · ·		· · ·
	Diff.	−1.45	· · ·		· · ·		· · ·
^{58}Ca	Calc.	455.31	3.595	0*f*	6.949	0*d*	5.221
	Exp.	452.71[b]	· · ·		· · ·		· · ·
	Diff.	2.60	· · ·		· · ·		· · ·
^{60}Ca	Calc.	463.74	3.609	1*p*	1.645	0*d*	5.216
	Exp.	· · ·	· · ·		· · ·		· · ·
	Diff.	· · ·	· · ·		· · ·		· · ·
^{70}Ca	Calc.	466.29	3.716	1*p*	1.560	0*d*	4.173
	Exp.	· · ·	· · ·		· · ·		· · ·
	Diff.	· · ·	· · ·		· · ·		· · ·
^{48}Ni	Calc.	351.41	3.779	0*d*	5.953	0*d*	5.803
	Exp.	347.56[b]	· · ·		· · ·		· · ·
	Diff.	3.85	· · ·		· · ·		· · ·
^{56}Ni	Calc.	481.85	3.774	0*d*	5.098	0*d*	5.207
	Exp.	483.99	3.727[c]		· · ·		· · ·
	Diff.	−2.14	0.047		· · ·		· · ·
^{60}Ni	Calc.	518.84	3.791	0*d*	5.423	0*d*	5.388
	Exp.	526.85	3.797		· · ·		· · ·
	Diff.	−8.01	−0.006		· · ·		· · ·
^{66}Ni	Calc.	575.30	3.866	0*f*	7.200	0*f*	4.617
	Exp.	576.83	· · ·		· · ·		· · ·
	Diff.	−1.53	· · ·		· · ·		· · ·
^{68}Ni	Calc.	591.52	3.878	1*p*	1.735	0*d*	4.658
	Exp.	590.43	· · ·		· · ·		· · ·
	Diff.	1.09	· · ·		· · ·		· · ·
^{78}Ni	Calc.	643.51	3.969	1*p*	1.562	0*d*	3.731
	Exp.	642.09[b]	· · ·		· · ·		· · ·
	Diff.	1.42	· · ·		· · ·		· · ·

TABLE VIII. (*Continued*).

Nucleus		E_B (MeV)	$\langle r^2 \rangle^{1/2}_{\text{charge}}$ (fm)	Neutron shell	$\Delta E^{(n)}_{\text{s.o.}}$ (MeV)	Proton shell	$\Delta E^{(p)}_{\text{s.o.}}$ (MeV)
^{60}Ge	Calc.	480.64	3.956	0*d*	5.250	0*d*	5.455
	Exp.	487.02	. . .		. . .		. . .
	Diff.	−6.38	. . .		. . .		. . .
^{82}Ge	Calc.	692.45	4.067	1*p*	2.025	0*d*	4.128
	Exp.	702.36	. . .		. . .		. . .
	Diff.	−9.91	. . .		. . .		. . .
^{90}Zr	Calc.	785.15	4.259	1*p*	1.911	1*p*	1.846
	Exp.	783.90	4.258		0.507		1.507
	Diff.	1.25	0.001		1.404		0.339
^{88}Sn	Calc.	617.69	4.478	0*f*	5.819	1*p*	1.785
	Exp.	. . .	. . .		. . .		. . .
	Diff.	. . .	. . .		. . .		. . .
^{90}Sn	Calc.	656.66	4.478	1*p*	1.838	1*p*	1.799
	Exp.	. . .	. . .		. . .		. . .
	Diff.	. . .	. . .		. . .		. . .
^{100}Sn	Calc.	830.99	4.496	1*p*	1.677	1*p*	1.649
	Exp.	823.29[b]	. . .		. . .		. . .
	Diff.	7.61	. . .		. . .		. . .
^{106}Sn	Calc.	885.70	4.521	1*p*	1.552	1*p*	1.657
	Exp.	893.87	. . .		. . .		. . .
	Diff.	−8.17	. . .		. . .		. . .
^{114}Sn	Calc.	970.56	4.601	0*g*	6.921	1*p*	1.505
	Exp.	971.58	4.602		. . .		. . .
	Diff.	−1.02	−0.001		. . .		. . .
^{116}Sn	Calc.	985.27	4.610	0*g*	6.851	1*p*	1.885
	Exp.	988.69	4.627		. . .		. . .
	Diff.	−3.42	−0.017		. . .		. . .
^{120}Sn	Calc.	1015.33	4.635	1*d*	2.326	1*p*	1.672
	Exp.	1020.55	4.643		. . .		. . .
	Diff.	−5.22	−0.008		. . .		. . .
^{132}Sn	Calc.	1104.45	4.721	1*d*	2.185	1*p*	1.454
	Exp.	1102.92	4.775[d]		. . .		. . .
	Diff.	−1.53	−0.054		. . .		. . .
^{140}Ce	Calc.	1177.70	4.887	1*d*	2.047	0*g*	5.899
	Exp.	1172.71	4.911[e]		. . .		. . .
	Diff.	4.99	−0.024		. . .		. . .
^{146}Gd	Calc.	1206.24	4.971	1*d*	2.330	0*g*	5.897
	Exp.	1204.45	5.034[f]		. . .		. . .
	Diff.	1.79	−0.063		. . .		. . .
^{158}Os	Calc.	1221.06	5.191	1*d*	2.108	0*g*	5.303
	Exp.	1214.89[b]	. . .		. . .		. . .
	Diff.	6.17	. . .		. . .		. . .
^{200}Os	Calc.	1564.08	5.459	1*f*	2.241	0*g*	4.124
	Exp.	1574.66[b]	. . .		. . .		. . .
	Diff.	−10.58	. . .		. . .		. . .

TABLE VIII. (*Continued*).

Nucleus		E_B (MeV)	$\langle r^2 \rangle^{1/2}_{\text{charge}}$ (fm)	Neutron shell	$\Delta E^{(n)}_{\text{s.o.}}$ (MeV)	Proton shell	$\Delta E^{(p)}_{\text{s.o.}}$ (MeV)
^{202}Os	Calc.	1575.48	5.467	2*p*	0.526	0*g*	4.106
	Exp.	1585.70[b]	· · ·		· · ·		· · ·
	Diff.	−10.22	· · ·		· · ·		· · ·
^{162}Hg	Calc.	1217.51	5.247	1*d*	2.041	1*d*	2.008
	Exp.	· · ·	· · ·		· · ·		· · ·
	Diff.	· · ·	· · ·		· · ·		· · ·
^{170}Hg	Calc.	1290.65	5.280	1*d*	1.836	1*d*	1.948
	Exp.	1302.17[b]	· · ·		· · ·		· · ·
	Diff.	−11.52	· · ·		· · ·		· · ·
^{204}Hg	Calc.	1604.77	5.492	1*f*	2.421	1*d*	1.672
	Exp.	1608.69	· · ·		· · ·		· · ·
	Diff.	−3.92	· · ·		· · ·		· · ·
^{206}Hg	Calc.	1617.82	5.499	2*p*	0.378	1*d*	1.768
	Exp.	1621.08	· · ·		· · ·		· · ·
	Diff.	−3.26	· · ·		· · ·		· · ·
^{164}Pb	Calc.	1212.88	5.272	1*d*	2.229	1*d*	2.175
	Exp.	· · ·	· · ·		· · ·		· · ·
	Diff.	· · ·	· · ·		· · ·		· · ·
^{172}Pb	Calc.	1290.50	5.302	1*d*	2.047	1*d*	2.139
	Exp.	· · ·	· · ·		· · ·		· · ·
	Diff.	· · ·	· · ·		· · ·		· · ·
^{182}Pb	Calc.	1412.60	5.377	0*h*	6.429	1*d*	2.009
	Exp.	1411.66	· · ·		· · ·		· · ·
	Diff.	0.94	· · ·		· · ·		· · ·
^{196}Pb	Calc.	1539.99	5.457	0*h*	5.797	1*d*	1.785
	Exp.	1543.25	· · ·		· · ·		· · ·
	Diff.	−3.26	· · ·		· · ·		· · ·
^{200}Pb	Calc.	1571.15	5.471	0*h*	5.718	1*d*	2.060
	Exp.	1576.41	· · ·		· · ·		· · ·
	Diff.	−5.26	· · ·		· · ·		· · ·
^{206}Pb	Calc.	1621.36	5.504	1*f*	2.506	1*d*	1.869
	Exp.	1622.36	5.490		· · ·		· · ·
	Diff.	−1.00	0.014		· · ·		· · ·

[a]Interpolation between experimental data points for ^{7}Li and ^{9}Be from Ref. [26].
[b]Calculated binding energy from Ref. [22].
[c]Extrapolation of experimental data point for ^{58}Ni from Ref. [26].
[d]Extrapolation of experimental data point for ^{124}Sn from Ref. [26].
[e]Extrapolation of experimental data point for ^{142}Nd from Ref. [26].
[f]Extrapolation of experimental data point for ^{154}Gd from Ref. [26].

For $A \geq 16$ we used Ref. [22] as the source of quadrupole deformations (from fitting experimental ground-state masses). Four of the nuclei chosen exceed the constraint $|\epsilon_2| \leq 0.05$ and instead lie in the range $0.050 \leq |\epsilon_2| \leq 0.084$. These are ^{34}Ca, ^{60}Ni, ^{60}Ge, and ^{170}Hg. For $A < 16$ the quadrupole deformations were obtained from the literature or are unknown. Some of the nuclei with $A > 16$ also have unknown deformation prop-

erties. These are ^{20}C, ^{22}C, ^{20}Si, ^{60}Ca, ^{70}Ca, ^{88}Sn, ^{90}Sn, ^{162}Hg, and ^{164}Pb. For our present purpose we assume that these are spherical nuclei.

The intersection of Set 1 and Set 2 yields a set of 58 nuclei within the ranges $2 \leq Z \leq 82$ and $4 \leq A \leq 208$. Three of these nuclei (^{16}O, ^{88}Sr, and ^{208}Pb) were used to determine the coupling constants to be tested (Table IV) and are therefore excluded. One nucleus, doubly magic ^{10}O, does not admit a bound-state solution with the coupling constants of Table IV. This leaves 54 nuclei to test the relativistic point coupling model.

B. Predicted observables

Comparisons of predicted and measured observables for 54 nuclei are given in Table VIII. The observables chosen are the same as those chosen to optimize the coupling constants (Table V), namely, the ground state binding energy, the root-mean-square charge radius, the energy splitting of the least-bound neutron spin-orbit pair, and the same for the least-bound proton spin-orbit pair. The average absolute deviations of the predicted observables from the measured observables for the nuclei of Table VIII with $A > 10$, 50 nuclei, are given in Table IX. Finally, the predicted root-mean-square radii of the point neutron and point proton densities, ρ_V^n and ρ_V^p, of all 54 nuclei are given in Table X.

While it is not expected that a mean-field approximation should be a viable approach for very light nuclei, it is nevertheless of interest to see how such an approximation breaks down in this region. We find for ^{8}He that the experimental binding energy is reasonably well predicted (8%), but that the rms charge radius is grossly underpredicted (23%). For ^{4}He, on the other hand, the experimental binding energy is predicted rather well (2%), but the rms charge radius is grossly overpredicted (27%). Given these strong fluctuations in calculated rms charge radii for ^{4}He and ^{8}He, we conclude that the relativistic point coupling model may be inappropriate for nuclei with, for example, $A \leq 10$. For this reason the average absolute deviations of Table IX are restricted to nuclei with $A > 10$. [Note that the center-of-mass correction to the rms charge radius, which we have neglected, is always in the direction to *reduce* the value obtained from Eq. (27)].

Table VIII shows that the observables for two very well studied nuclei, ^{40}Ca and ^{48}Ca, are predicted reasonably well by our model. Their binding energies are pre-

TABLE IX. Average absolute deviations[a,b] of predicted observables from measured observables for nuclei with $A > 10$.

Observable X	Average absolute deviation $\langle \delta X \rangle$	Number of cases N_X
E_B	2.783 MeV	32
$\langle r^2 \rangle_{\text{charge}}^{1/2}$	0.021 fm	14
$\Delta E_{\text{s.o.}}^{(n)}$	1.409 MeV	3
$\Delta E_{\text{s.o.}}^{(p)}$	0.844 MeV	3

[a]Not including the observables for the nuclei used to optimize the coupling constants.

[b]$\langle \delta X \rangle = (1/N_X) \sum_{i=1}^{N_X} |X_{\text{calc}}^{(i)} - X_{\text{exp}}^{(i)}|$.

TABLE X. Predicted root-mean-square radii of point neutron and point proton densities.

Nucleus	$\langle r^2 \rangle_n^{1/2}$ (fm)	$\langle r^2 \rangle_p^{1/2}$ (fm)
^{4}He	1.997	2.011
^{8}He	2.772	1.936
^{10}He	3.046	1.987
^{8}C	1.937	2.939
^{14}C	2.622	2.472
^{20}C	3.133	2.523
^{22}C	3.349	2.544
^{14}O	2.456	2.661
^{22}O	3.048	2.649
^{24}O	3.239	2.666
^{28}O	3.465	2.751
^{20}Si	2.515	3.286
^{22}Si	2.637	3.125
^{34}Si	3.312	3.103
^{36}S	3.306	3.208
^{34}Ca	3.081	3.388
^{40}Ca	3.329	3.374
^{48}Ca	3.627	3.410
^{52}Ca	3.823	3.437
^{58}Ca	4.019	3.536
^{60}Ca	4.097	3.552
^{70}Ca	4.358	3.669
^{48}Ni	3.384	3.705
^{56}Ni	3.656	3.704
^{60}Ni	3.802	3.723
^{66}Ni	3.974	3.803
^{68}Ni	4.036	3.816
^{78}Ni	4.285	3.914
^{60}Ge	3.681	3.887
^{82}Ge	4.281	4.010
^{90}Zr	4.315	4.201
^{88}Sn	4.118	4.416
^{90}Sn	4.154	4.416
^{100}Sn	4.366	4.437
^{106}Sn	4.501	4.465
^{114}Sn	4.660	4.548
^{116}Sn	4.703	4.557
^{120}Sn	4.784	4.583
^{132}Sn	4.982	4.673
^{140}Ce	5.021	4.838
^{146}Gd	5.032	4.922
^{158}Os	5.089	5.141
^{200}Os	5.690	5.417
^{202}Os	5.717	5.425
^{162}Hg	5.110	5.197
^{170}Hg	5.231	5.231
^{204}Hg	5.694	5.450
^{206}Hg	5.719	5.457
^{164}Pb	5.116	5.222
^{172}Pb	5.235	5.254
^{182}Pb	5.379	5.330
^{196}Pb	5.574	5.413
^{200}Pb	5.620	5.427
^{206}Pb	5.692	5.461

dicted to within 1.2 MeV, their rms charge radii to within 0.03 fm, and the spin-orbit splittings are predicted to within about 0.5 MeV for ^{40}Ca, and to within about 2 MeV for ^{48}Ca. Turning to the corresponding rms radii of the neutron and proton point densities in Table X, one observes that the protons in ^{40}Ca are, on average, 0.045 fm outside of the neutrons and that in ^{48}Ca the neutrons are, on average, 0.217 fm outside of the protons, in good agreement with recent analyses of elastic pion scattering experiments [31].

It is also interesting to note from Table VIII that the exotic doubly magic nuclei ^{28}O, ^{70}Ca, ^{48}Ni, ^{78}Ni, ^{100}Sn, ^{132}Sn, and ^{164}Pb are not only bound, but appear to possess reasonable ground state properties as well.

The average absolute deviations of the predicted observables from the measured observables for the nuclei of Table VIII with $A > 10$ are given in Table IX. The average absolute deviation for the binding energies is about 2.8 MeV, which is quite respectable for a first attempt, we believe, but nevertheless is a factor of three worse than the most modern Schrödinger-equation based mass formulas with many more constants (see Ref. [22], for example). Part of the reason for not doing better may be the severity of allowing orbital occupation probabilities of only 0 or 1 in the present form of our program. On the other hand, the average absolute deviation of the rms charge radii is about 0.02 fm, a result that may be better than we should expect given the same severe limitation on orbital occupation probabilities. The average absolute deviations in the spin-orbit splittings are more difficult to assess because they are so few in number and because they are so difficult to extract from experiment. Nevertheless, it is clear that values of about 1.4 MeV for neutrons and 0.8 MeV for protons are small enough to conclude that the correct magnitude spin-orbit force appears naturally in the relativistic point coupling model. This conclusion is reinforced by inspecting Table V.

Predicted rms radii of the point neutron and point proton densities, ρ_V^n and ρ_V^p, are given in Table X. These rms radii are useful in assessing the neutron or proton "skins" given by their differences $\langle r^2\rangle_n^{1/2} - \langle r^2\rangle_p^{1/2}$ and $\langle r^2\rangle_p^{1/2} - \langle r^2\rangle_n^{1/2}$, respectively. We point out here the interesting ranges represented for the isotopic sequences ^{34}Ca$\rightarrow^{70}$Ca, ^{48}Ni$\rightarrow^{78}$Ni, ^{100}Sn$\rightarrow^{132}$Sn, and ^{164}Pb$\rightarrow^{208}$Pb (note that the ^{208}Pb values are given in Table VII). For example, the sequence $\{^{34}$Ca, ^{40}Ca, ^{48}Ca, ^{52}Ca, ^{58}Ca, ^{60}Ca, ^{70}Ca$\}$ begins with a proton "skin" of 0.307 fm and ends with a neutron "skin" of 0.689 fm. The smallest "skin" in the sequence, already mentioned earlier, is the proton "skin" of 0.045 fm for ^{40}Ca. Similarly, the sequence $\{^{48}$Ni, ^{56}Ni, ^{60}Ni, ^{66}Ni, ^{68}Ni, ^{78}Ni$\}$ begins with a proton "skin" of 0.321 fm and ends with a neutron "skin" of 0.371 fm. In this sequence, the smallest "skin" is the proton "skin" of 0.048 fm for ^{56}Ni. Doubly magic ^{164}Pb has a predicted proton "skin" of 0.106 fm.

C. Predicted densities and potentials for some representative nuclei

We show predictions of the neutron and proton point densities ρ_V^n and ρ_V^p, respectively, together with their sum

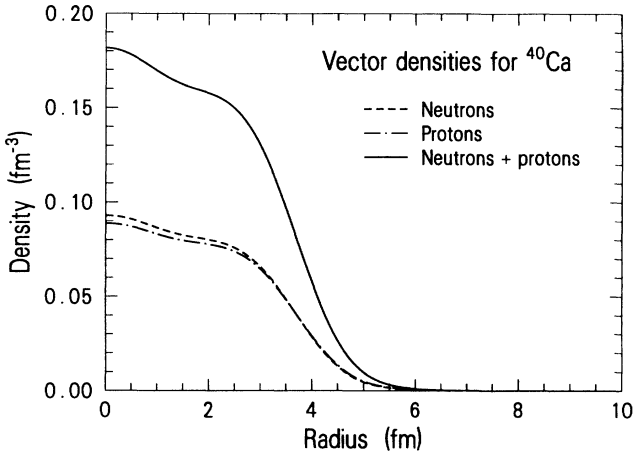

FIG. 19. Neutron and proton point densities $\rho_V^n(r)$ and $\rho_V^p(r)$, respectively, for ^{40}Ca. Their sum is the isoscalar-vector (baryon) density $\rho_V(r)$ for ^{40}Ca.

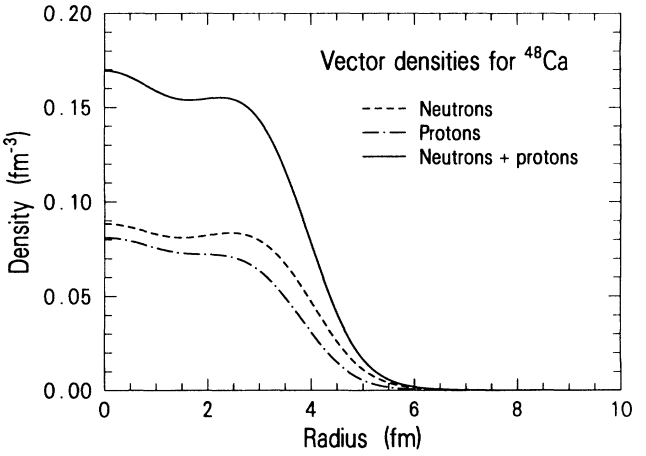

FIG. 20. Neutron and proton point densities $\rho_V^n(r)$ and $\rho_V^p(r)$, respectively, for ^{48}Ca. Their sum is the isoscalar-vector (baryon) density $\rho_V(r)$ for ^{48}Ca.

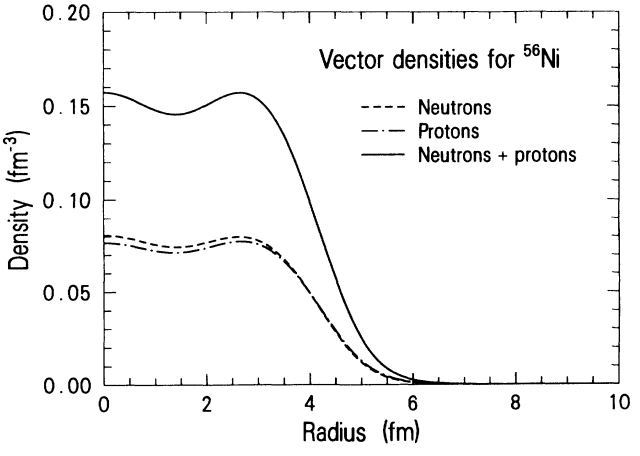

FIG. 21. Neutron and proton point densities $\rho_V^n(r)$ and $\rho_V^p(r)$, respectively, for ^{56}Ni. Their sum is the isoscalar-vector (baryon) density $\rho_V(r)$ for ^{56}Ni

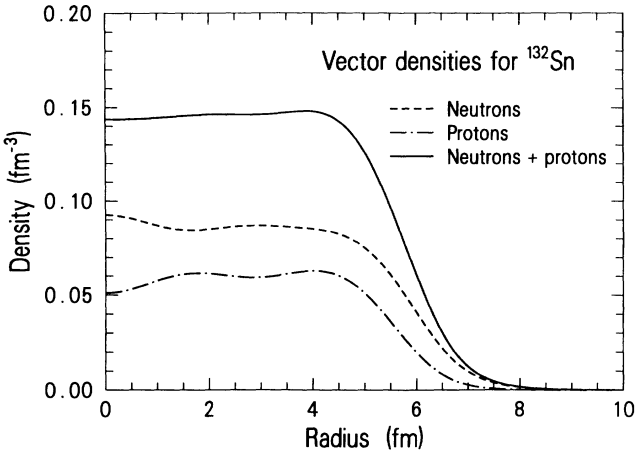

FIG. 22. Neutron and proton point densities $\rho_V^n(r)$ and $\rho_V^p(r)$, respectively, for ^{132}Sn. Their sum is the isoscalar-vector (baryon) density $\rho_V(r)$ for ^{132}Sn.

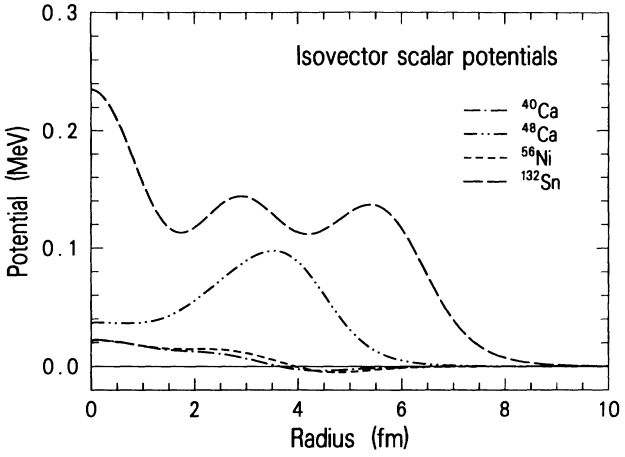

FIG. 24. Isovector-scalar potentials $V_{TS}(r)$ for ^{40}Ca, ^{48}Ca, ^{56}Ni, and ^{132}Sn.

the isoscalar-vector (baryon) density ρ_V, for the four representative nuclei, ^{40}Ca, ^{48}Ca, ^{56}Ni, and ^{132}Sn, in Figs. 19–22. The central vector density for ^{40}Ca exceeds 0.18 fm^{-3}, but falls off very fast to 0.16 fm^{-3} at about 1.7 fm. The point neutron density exceeds the point proton density except in the tail region where the converse is true. In ^{48}Ca a minimum exists in the vector density at about 1.5 fm, due primarily to neutron contributions. Here the point neutron density exceeds the point proton density, as expected, for all values of r. A minimum also exists in the vector density for ^{56}Ni, at about 1.3 fm, followed by a rather substantial maximum at about 2.6 fm. This structure is due to comparable contributions from both the point neutron and point proton densities. As in the other $N=Z$ nucleus ^{40}Ca, the point proton density exceeds the point neutron density in the tail region. The vector density for ^{132}Sn has a shallow minimum at the origin and a weak maximum at about 4 fm. However, the point neutron and point proton densities show quite dramatic structure with several minima and maxima, especially at the origin where the neutron and proton densities are just under a factor of two apart.

The predicted isoscalar-scalar potentials V_S, isoscalar-vector potentials V_V, isovector-scalar potentials V_{TS}, and isovector-vector potentials V_{TV} are shown in Figs. 23–25 for the same four representative nuclei. The behavior of the isoscalar potentials is similar to those of Fig. 9, but it is interesting to note that the magnitudes of the ^{132}Sn potentials, in the central region, are less than those of the $0f_{7/2}$ shell nuclei shown. Also, the isoscalar-vector potentials (and isoscalar-scalar potentials) for the $0f_{7/2}$ shell nuclei shown, cross each other at radii located between 2.0 and 2.5 fm. The isovector-scalar potentials are similar in overall magnitudes to those of Fig. 10, but the structure of these potentials is highly specific to each nucleus. The $N=Z$ nuclei, ^{40}Ca and ^{56}Ni, exhibit similar behavior reflecting the slight dominance of the proton point density over the neutron point density in the surface regions and the converse in the interior regions. The dramatic structure seen for ^{48}Ca and ^{132}Sn simply represents the large difference between the neutron and proton point densities for these nuclei, shown in Figs. 20

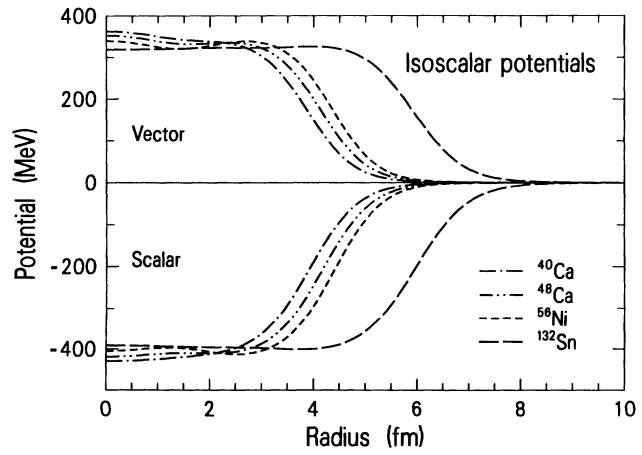

FIG. 23. Isoscalar-scalar and isoscalar-vector potentials $V_S(r)$ and $V_V(r)$, respectively, for ^{40}Ca, ^{48}Ca, ^{56}Ni, and ^{132}Sn.

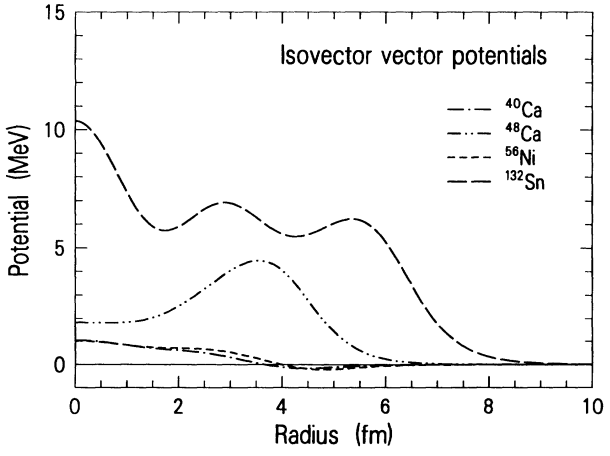

FIG. 25. Isovector-vector potentials $V_{TV}(r)$ for ^{40}Ca, ^{48}Ca, ^{56}Ni, and ^{132}Sn.

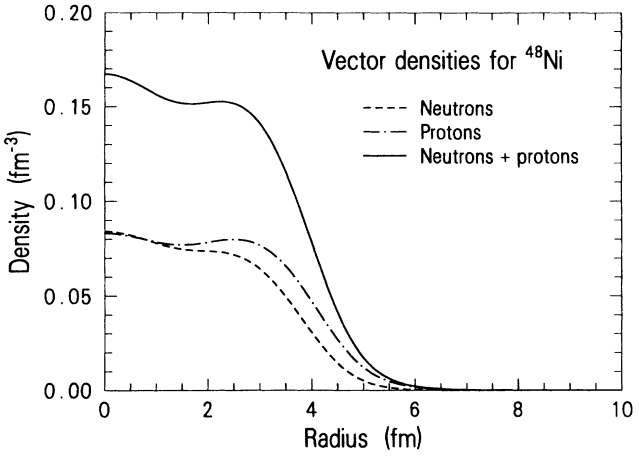

FIG. 26. Neutron and proton point densities $\rho_V^n(r)$ and $\rho_V^p(r)$, respectively, for ^{48}Ni. Their sum is the isoscalar-vector (baryon) density $\rho_V(r)$ for ^{48}Ni.

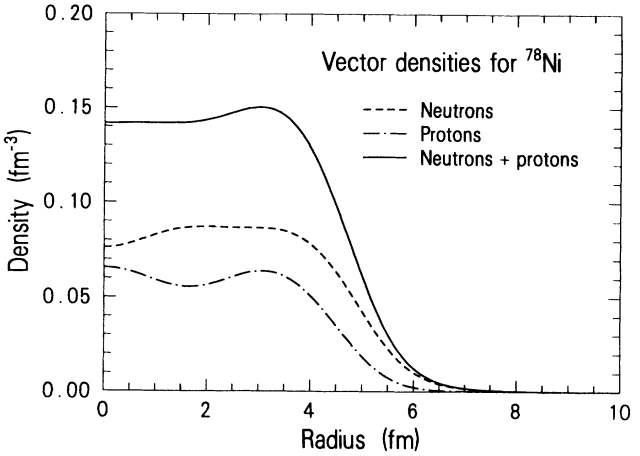

FIG. 28. Neutron and proton point densities $\rho_V^n(r)$ and $\rho_V^p(r)$, respectively, for ^{78}Ni. Their sum is the isoscalar-vector (baryon) density $\rho_V(r)$ for ^{78}Ni.

and 22 [see Eq. (35)]. An entirely similar set of remarks holds for the isovector-vector potentials shown in Fig. 25. Note, moreover, that the overall magnitudes of the isovector-vector potentials are similar to those of Fig. 11 and, again, the isovector-vector potentials dominate the isovector-scalar potentials by a factor of approximately 50.

D. Predicted densities and potentials for some exotic nuclei

In this subsection we consider the four exotic doubly magic nuclei ^{48}Ni, ^{70}Ca, ^{78}Ni, and ^{100}Sn. Little is known about these nuclei, including whether or not they are bound. Our calculations indicate that they are bound. From Table VIII we extract the predicted values of the binding energy per nucleon, E_B/A, for the four, namely, 7.321, 6.661, 8.250, and 8.309 MeV, respectively.

Predicted neutron and proton point densities ρ_V^n and ρ_V^p, respectively, together with their sum the isoscalar-

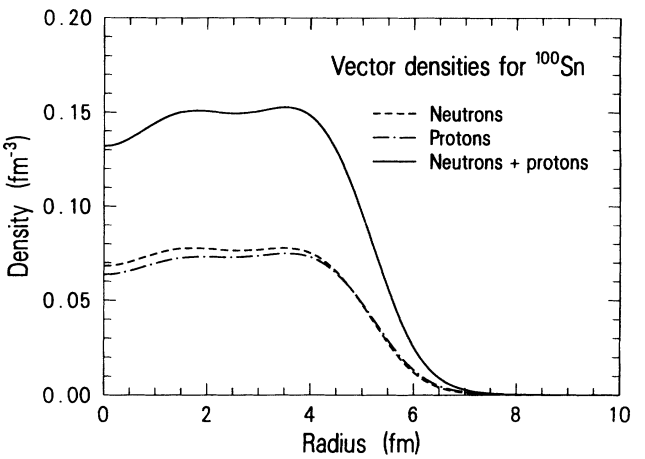

FIG. 29. Neutron and proton point densities $\rho_V^n(r)$ and $\rho_V^p(r)$, respectively, for ^{100}Sn. Their sum is the isoscalar-vector (baryon) density $\rho_V(r)$ for ^{100}Sn.

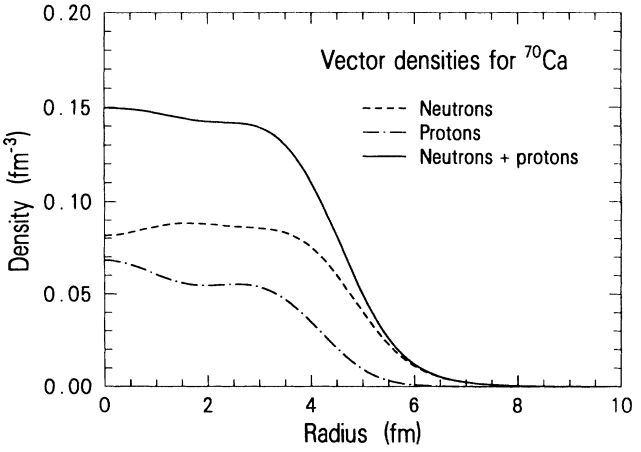

FIG. 27. Neutron and proton point densities $\rho_V^n(r)$ and $\rho_V^p(r)$, respectively, for ^{70}Ca. Their sum is the isoscalar-vector (baryon) density $\rho_V(r)$ for ^{70}Ca.

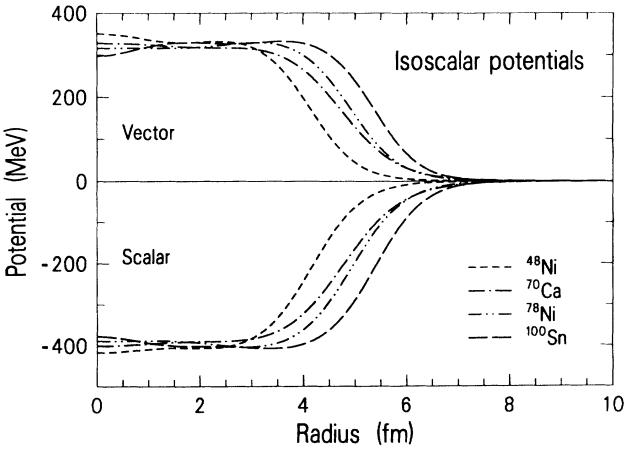

FIG. 30. Isoscalar-scalar and isoscalar-vector potentials $V_S(r)$ and $V_V(r)$, respectively, for ^{48}Ni, ^{70}Ca, ^{78}Ni, and ^{100}Sn.

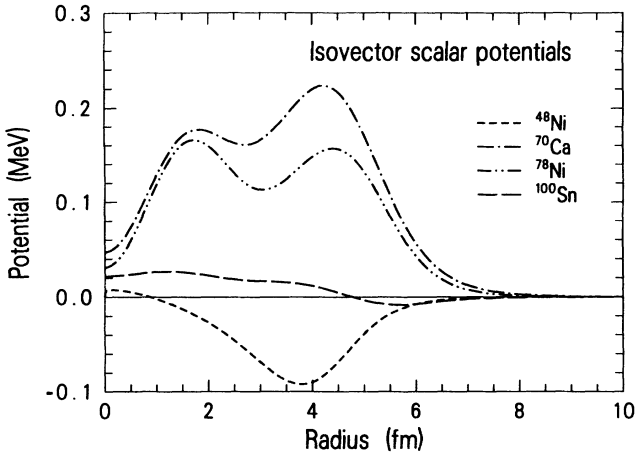

FIG. 31. Isovector-scalar potentials $V_{TS}(r)$ for ^{48}Ni, ^{70}Ca, ^{78}Ni, and ^{100}Sn.

vector density ρ_V, are shown for the four exotic nuclei in Figs. 26–29. Likewise, the predicted isoscalar-scalar potentials V_S, isoscalar-vector potentials V_V, isovector-scalar potentials V_{TS}, and isovector-vector potentials V_{TV} are shown for the same four nuclei in Figs. 30–32. In particular, Figs. 31 and 32 demonstrate the effects of large changes in the neutron excess (nuclear isospin) upon the magnitudes and shapes of the isovector potentials V_{TS} and V_{TV}. In this example, the neutron excess $N-Z$ ranges from -8, for ^{48}Ni to $+30$, for ^{70}Ca.

It is instructive to compare the rms radii of the point neutron and point proton densities for these nuclei, from Table X, with the actual point densities themselves shown in Figs. 26–29. In particular, the much larger neutron "skin" of ^{70}Ca in comparison with that of ^{78}Ni (both nuclei with $N=50$) is explained, that is, the eight $0f_{7/2}$ protons in ^{78}Ni are mainly responsible for the difference, as the two point neutron densities are almost the same.

The differences observed between the point neutron and point proton densities for ^{48}Ni are responsible, through Eq. (35), for the relatively large negative peaks in

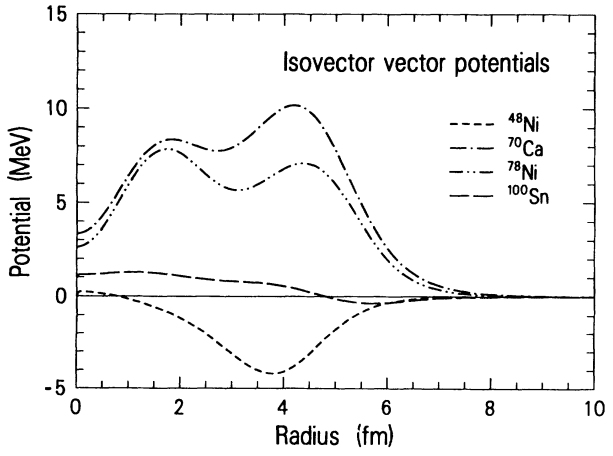

FIG. 32. Isovector-vector potentials $V_{TV}(r)$ for ^{48}Ni, ^{70}Ca, ^{78}Ni, and ^{100}Sn.

the isovector potentials for this nucleus, shown in Figs. 31 and 32. The isoscalar potentials, Fig. 30, are similar to those shown previously. Note, however, the differences in slope for the isotones ^{70}Ca and ^{78}Ni.

E. Nuclear matter

As a final test in our first study of the relativistic point coupling model we calculate some of the properties of saturated nuclear matter, that is, at the minimum in the equation of state for nuclear matter. Analogous to Eqs. (21)–(23) for finite nuclei, we now consider all diagonal elements of the energy-momentum density tensor $T_{\mu\nu}$ and calculate the energy density of nuclear matter, $\mathcal{E}$, as a function of nuclear matter density [14]. The minimum in this equation of state, $\mathcal{E}(\rho_{NM})$, is the saturation point, the so-called "ground state" of nuclear matter.

We use our optimized set of coupling constants from Table IV and consider nuclear matter with no Coulomb forces. Accordingly, we set $\delta_S \equiv \delta_V \equiv 0.0$ and are left with the remaining seven coupling constants from the table, namely, α_S, β_S, γ_S, α_V, γ_V, α_{TS}, and α_{TV}. In addition, for these calculations we define the nucleon mass m as

$$m=\tfrac{1}{2}(m_n+m_p)=938.926 \text{ MeV} . \tag{41}$$

We find the minimum in $\mathcal{E}(\rho_{NM})$ at $\rho_{NM}=0.148$ fm^{-3}, which corresponds to a Fermi wave number for the nucleon of 1.299 fm^{-1} through the relation

$$\rho_{NM}=\frac{\nu}{6\pi^2}k_F^3 , \tag{42}$$

where the spin-isospin degeneracy ν has the value 4 for nuclear matter. The magnitude of the energy density $\mathcal{E}$ at the minimum (binding energy/nucleon) is 16.126 MeV. We calculate the compressibility of nuclear matter, K, with the relation

$$K=k_F^2\frac{\partial^2}{\partial k_F^2}\mathcal{E}(k_F) , \tag{43}$$

evaluated at the minimum and find $K=264.032$ MeV. We also calculate the symmetry energy, a_4, using the relation

$$a_4=\frac{1}{2}\frac{\partial^2}{\partial\delta^2}\mathcal{E}(\rho_V^n,\rho_V^p) , \tag{44}$$

where

$$\delta=\frac{\rho_V^n-\rho_V^p}{\rho_V^n+\rho_V^p} , \tag{45}$$

TABLE XI. Properties of saturated nuclear matter.

Quantity	Magnitude
Fermi wave number k_F	1.299 fm^{-1}
Density ρ_{NM}	0.148 fm^{-3}
Binding energy/nucleon $\mathcal{E}$	16.126 MeV
Compressibility K	264.032 MeV
Symmetry energy/nucleon a_4	37.194 MeV
Effective mass m^*/m	0.575

and the derivative is calculated under the constraint $\rho_V^n+\rho_V^p=\text{const}=2\rho_{NM}$. We find $a_4=37.194$ MeV. Lastly, we determine the effective nucleon mass in the medium, m^*, through the relation

$$m^*=m+V_S(\alpha_S,\beta_S,\gamma_S)\ , \tag{46}$$

and find $m^*/m=0.575$. All of the results here are summarized in Table XI.

In comparing these results with other relativistic mean field calculations of saturated nuclear matter, we find quite good agreement. In particular, all properties in Table XI, including the compressibility K, agree well with the results of Reinhard [11] for nonlinear scalar field calculations performed with his own meson parameters as well as with meson parameter sets obtained from Boussy *et al.* [4,5]. The nuclear matter properties in Table XI are also consistent with those determined by Horowitz and Serot [3], except for the compressibility K where their value is about double ours.

VI. DISCUSSION AND CONCLUSIONS

We have investigated a new relativistic point coupling model that is comprised of mean nucleon fields where the corresponding densities are of scalar and vector character each having isoscalar and isovector components. No explicit mean meson fields appear in the model. The nine coupling constants of the model have been determined by reproducing measured ground state observables for three closed-shell nuclei, simultaneously, in a nonlinear least-squares adjustment algorithm. The three nuclei chosen were doubly magic ^{16}O and ^{208}Pb, and singly magic ^{88}Sr, which is closed subshell in proton number. The predictive power of the model has been tested by calculating the same observables, and others, for 54 other closed shell nuclei and by calculation of a number of properties of saturated nuclear matter. *The results are better than we had hoped and they provide incentive to continue development of the model.*

Specifically, the model in its present form predicts the ground state binding energy and rms charge radius well, particularly the latter, and it obtains the correct spin-orbit splitting in some cases, while at least obtaining the correct magnitude in others. Part of the problem with this latter observable is that it is difficult to extract from experiment except in some isolated cases (^{16}O and ^{208}Pb, for example). The rather good agreement with the results of relativistic mean meson field approaches for the properties of saturated nuclear matter was obtained after the coupling constants of Table IV were determined, that is, *our nuclear matter calculations were performed without any parameter adjustment whatsoever.*

We have learned that the mean nucleon fields generated by this relativistic point coupling approach may be inappropriate for finite nuclei with $A<\sim 10$, based upon calculations for ^{4}He and ^{8}He. We have also learned that the nine coupling constants of the model can possibly be reduced to eight, that is, it may be possible to set the isovector-scalar coupling constant, α_{TS}, identically to zero. This is based upon the observation that α_{TS} is only $\sim 2\%$ of the magnitude of the isovector-vector coupling constant α_{TV}. Insofar as the isovector-scalar and isovector-vector mean nucleon fields correspond to the mean meson fields for the δ and ρ mesons, respectively, setting $\alpha_{TS}=0$ is equivalent to ignoring δ meson exchange, which is precisely what is done in most of the successful mean meson field approaches.

In our future work we will first introduce orbital occupation probabilities based upon the BCS pairing approach [32], instead of using the fixed occupation probabilities of 0 and 1. This will broaden the range of nuclei that can be addressed and should improve our predictive capability. Second, we intend to introduce the deformation degrees of freedom, which further broadens the range of nuclei that can be calculated, but requires the construction of an entirely new computer code. Finally, we hope to include an explicit treatment of exchange processes.

ACKNOWLEDGMENTS

We are grateful to J. Friar, T. Goldman, P. Manakos, J. R. Nix, P.-G. Reinhard, and D. Strottman for stimulating discussions. Two of us (B.A.N. and T.H.) wish to thank the Theoretical Division of the Los Alamos National Laboratory for their hospitality and support during our respective visits. This work was supported by the U.S. Department of Energy, the Technische Hochschule Darmstadt, and the Deutsche Forschungsgemeinschaft.

[1] R. Brockmann and W. Weise, Phys. Rev. C **16**, 1282 (1977).
[2] B. D. Serot and J. D. Walecka, Phys. Lett. **87B**, 172 (1979).
[3] C. J. Horowitz and B. D. Serot, Nucl. Phys. **A368**, 503 (1981).
[4] A. Bouyssy, S. Marcos, and J. F. Mathiot, Nucl. Phys. **A415**, 497 (1984).
[5] A. Bouyssy, S. Marcos, and P. van Thieu, Nucl. Phys. **A422**, 541 (1984).
[6] B. D. Serot and J. D. Walecka, in *Advances in Nuclear Physics,* edited by J. W. Negele and E. Vogt (Plenum, New York, 1986), Vol. 16, p. 1.
[7] P.-G. Reinhard, M. Rufa, J. Maruhn, W. Greiner, and J. Friedrich, Z. Phys. A **323**, 13 (1986).
[8] A. Bouyssy, J.-F. Mathiot, Nguyen Van Giai, and S. Marcos, Phys. Rev. C **36**, 380 (1987).
[9] P. G. Blunden and M. J. Iqbal, Phys. Lett. **196B**, 295 (1987).
[10] M. Rufa, P.-G. Reinhard, J. A. Maruhn, W. Greiner, and M. R. Strayer, Phys. Rev. C **38**, 390 (1988).
[11] P.-G. Reinhard, Rep. Prog. Phys. **52**, 439 (1989).
[12] Y. K. Gambhir, P. Ring, and A. Thimet, Ann. Phys. **198**, 132 (1990).
[13] P. Manakos and T. Mannel, Z. Phys. A **330**, 223 (1988).
[14] C. Itzykson and J. Zuber, *Quantum Field Theory* (McGraw-Hill, New York, 1980), p. 22.
[15] P. Manakos and T. Mannel, Z. Phys. A **334**, 481 (1989).

[16] B. A. Nikolaus, D. G. Madland, and P. Manakos, Bull. Am. Phys. Soc. **35**, 976 (1990).
[17] T. Hoch, B. A. Nikolaus, and D. G. Madland, Bull. Am. Phys. Soc. **35**, 1651 (1990).
[18] P.-G. Reinhard, private communication.
[19] J. L. Friar and J. W. Negele, in *Advances in Nuclear Physics,* edited by M. Baranger and E. Vogt (Plenum, New York, 1975), Vol. 8, p. 219.
[20] J. R. Ford, W. R. Boland, J. Chow, V. Faber, P. O. Frederickson, T. L. Jordan, T. A. Manteuffel, and A. B. White, Jr., *Common Los Alamos Mathematical Software Compendium,* Los Alamos National Laboratory internal document (1987).
[21] J. J. More, in *Numerical Analysis,* edited by G. A. Watson (Springer-Verlag, New York, 1977), p. 630.
[22] P. Möller and J. R. Nix, At. Data Nucl. Data Tables **39**, 213 (1988).
[23] R. Kozack and D. G. Madland, Phys. Rev. C **39**, 1461 (1989).
[24] A. Bohr and B. Mottelson, *Nuclear Structure* (Benjamin, New York, 1969), Vol. 1.
[25] G. Audi, Midstream Atomic Mass Evaluation, private communication.
[26] H. deVries, C. W. Jager, and C. deVries, At. Data Nucl. Data Tables **36**, 495 (1987).
[27] X. Campi and D. W. Sprung, Nucl. Phys. **A194**, 401 (1972).
[28] C. M. Lederer and V. Shirley, Eds., *Table of Isotopes,* 7th ed. (Wiley, New York, 1978).
[29] M. R. Schmorak, Nucl. Data Sheets **43**, 383 (1984).
[30] R. Machleidt, in *Relativistic Dynamics and Quark-Nuclear Physics,* edited by M. B. Johnson and A. Picklesimer (Wiley, New York, 1986), p. 71.
[31] A. Hayes, private communication.
[32] J. Bardeen, L. N. Cooper, and J. R. Schrieffer, Phys. Rev. **108**, 1175 (1957).